

# Uncovering hidden geometry in Transformers via disentangling position and context

Jiajun Song\*, Yiqiao Zhong†

February 6, 2024

## Abstract

Transformers are widely used to extract semantic meanings from input tokens, yet they usually operate as black-box models. In this paper, we present a simple yet informative decomposition of hidden states (or embeddings) of trained transformers into interpretable components. For any layer, embedding vectors of input sequence samples are represented by a tensor  $\mathbf{h} \in \mathbb{R}^{C \times T \times d}$ . Given embedding vector  $\mathbf{h}_{c,t} \in \mathbb{R}^d$  at sequence position  $t \leq T$  in a sequence (or context)  $c \leq C$ , extracting the mean effects yields the decomposition

$$\mathbf{h}_{c,t} = \boldsymbol{\mu} + \mathbf{pos}_t + \mathbf{ctx}_c + \mathbf{resid}_{c,t}$$

where  $\boldsymbol{\mu}$  is the global mean vector,  $\mathbf{pos}_t$  and  $\mathbf{ctx}_c$  are the mean vectors across contexts and across positions respectively, and  $\mathbf{resid}_{c,t}$  is the residual vector. For popular transformer architectures and diverse text datasets, empirically we find pervasive mathematical structure: (1)  $(\mathbf{pos}_t)_t$  forms a low-dimensional, continuous, and often spiral shape across layers, (2)  $(\mathbf{ctx}_c)_c$  shows clear cluster structure that falls into context topics, and (3)  $(\mathbf{pos}_t)_t$  and  $(\mathbf{ctx}_c)_c$  are nearly orthogonal. We argue that smoothness is pervasive and beneficial to transformers trained on languages, and our decomposition leads to improved model interpretability.

## 1 Introduction

Transformers (Vaswani et al., 2017) are practical neural network models that underlie recent successes of large language models (LLMs) (Brown et al., 2020; Bubeck et al., 2023). Unfortunately, transformers are often used as black-box models due to lack of in-depth analyses of internal mechanism, which raises concerns such as lack of interpretability, model biases, security issues, etc., (Bommasani et al., 2021).

In particular, it is poorly understood what information embeddings from each layer capture. We identify two desiderata: (1) internal quantitative measurements, particularly for the intermediate layers; (2) visualization tools and diagnostics tailored to transformers beyond attention matrix plots.

Let us introduce basic notations. An input sequence consists of  $T$  consecutive tokens (e.g., words or subwords), and a corpus is a collection of all input sequences. Let  $C$  be the total number of input sequences and  $c \leq C$  denote a generic sequence, which may be represented by  $\mathbf{x}_{c,1}, \dots, \mathbf{x}_{c,T}$  where each

\*National Key Laboratory of General Artificial Intelligence, Beijing Institute for General Artificial Intelligence (BIGAI), Beijing 100080, China, songjiajun@bigai.ai

†Department of Statistics, University of Wisconsin–Madison, WI, 53706, USA, yiqiao.zhong@wisc.edu

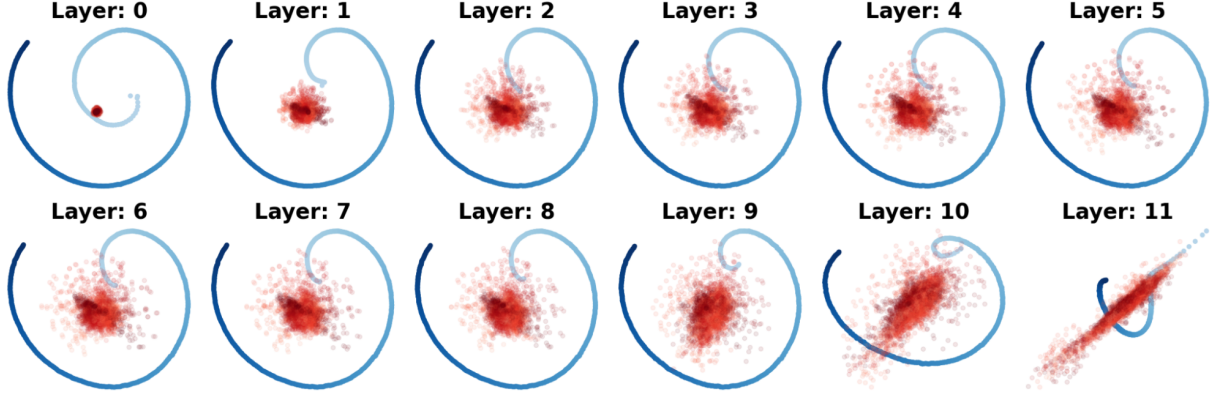


Figure 1: **PCA visualization** of positional basis (blue) and cvecs (red) from GPT-2 on OpenWebText. For every layer  $\ell$ , each  $\text{pos}_t^{(\ell)}$  and randomly selected  $\text{cvec}_{c,t}^{(\ell)}$  are projected using top-2 principal directions of  $(\text{pos}_t^{(\ell)})_{t \leq T}$ . Darker blue/red colors correspond to larger  $t$ . Principal components have dramatically **increasing scales** across layers, but for aesthetic purposes we rescaled all plots.

$\mathbf{x}_{c,t}$  corresponds to a token. We start from the initial static (and positional) embeddings  $(\mathbf{h}_{c,t}^{(0)})_{t \leq T}$  and then calculate the intermediate-layer embeddings  $(\mathbf{h}_{c,t}^{(\ell)})_{t \leq T}$ :

$$\begin{aligned} \mathbf{h}_{c,1}^{(0)}, \dots, \mathbf{h}_{c,T}^{(0)} &= \text{Embed}(\mathbf{x}_{c,1}, \dots, \mathbf{x}_{c,T}) \\ \mathbf{h}_{c,1}^{(\ell)}, \dots, \mathbf{h}_{c,T}^{(\ell)} &= \text{TFLayer}_{\ell}(\mathbf{h}_{c,1}^{(\ell-1)}, \dots, \mathbf{h}_{c,T}^{(\ell-1)}), \end{aligned}$$

for  $\ell = 1, \dots, L$ , where  $\text{Embed}$  and  $\text{TFLayer}_{\ell}$  are general mappings. This general definition encompasses many transformer models, which depend on attention heads defined as follows. Given  $d_{\text{head}} \leq d$  and input matrix  $\mathbf{X} \in \mathbb{R}^{T \times d}$ , for trainable weights  $\mathbf{W}^q, \mathbf{W}^k, \mathbf{W}^v \in \mathbb{R}^{d \times d_{\text{head}}}$ , define

$$\text{AttnHead}(\mathbf{X}) = \text{softmax}\left(\frac{\mathbf{X}\mathbf{W}^q(\mathbf{W}^k)^{\top}\mathbf{X}^{\top}}{\sqrt{d_{\text{head}}}}\right)\mathbf{X}\mathbf{W}^v. \quad (1)$$

Multi-head attention heads, denoted by MHA, are essentially the concatenation of many attention heads. Denote a generic fully-connected layer by  $\text{FFN}(\mathbf{x}) = \mathbf{W}_2 \max\{\mathbf{0}, \mathbf{W}_1 \mathbf{x} + \mathbf{b}_1\} + \mathbf{b}_2$  given any  $\mathbf{x} \in \mathbb{R}^d$  for trainable weights  $\mathbf{W}_1 \in \mathbb{R}^{d' \times d}$ ,  $\mathbf{W}_2 \in \mathbb{R}^{d \times d'}$ ,  $\mathbf{b}_1 \in \mathbb{R}^{d'}$ ,  $\mathbf{b}_2 \in \mathbb{R}^d$  (often  $d' = 4d$ ), and let LN be a generic layer normalization layer. The standard transformer is expressed as

$$\begin{aligned} \mathbf{h}_c^{(\ell+0.5)} &= \mathbf{h}_c^{(\ell)} + \text{MHA}^{(\ell)}(\text{LN}^{(\ell,1)}(\mathbf{h}_c^{(\ell)})), \\ \mathbf{h}_c^{(\ell+1)} &= \mathbf{h}_c^{(\ell+0.5)} + \text{FFN}^{(\ell)}(\text{LN}^{(\ell,2)}(\mathbf{h}_c^{(\ell+0.5)})) \end{aligned}$$

where  $\mathbf{h}_c^{(\ell+0.5)} = (\mathbf{h}_{c,1}^{(\ell+0.5)}, \dots, \mathbf{h}_{c,T}^{(\ell+0.5)})$  and  $\mathbf{h}_c^{(\ell)} = (\mathbf{h}_{c,1}^{(\ell)}, \dots, \mathbf{h}_{c,T}^{(\ell)})$ .

## 1.1 A mean-based decomposition

For each embedding vector  $\mathbf{h}_{c,t}^{(\ell)} \in \mathbb{R}^d$  from any trained transformer, consider the decomposition

$$\mathbf{h}_{c,t}^{(\ell)} = \boldsymbol{\mu}^{(\ell)} + \text{pos}_t^{(\ell)} + \text{ctx}_c^{(\ell)} + \text{resid}_{c,t}^{(\ell)}, \quad (2)$$

$$\boldsymbol{\mu}^{(\ell)} := \frac{1}{CT} \sum_{c,t} \mathbf{h}_{c,t}^{(\ell)}, \quad \mathbf{pos}_t^{(\ell)} := \frac{1}{C} \sum_c \mathbf{h}_{c,t}^{(\ell)} - \boldsymbol{\mu}^{(\ell)}, \quad (3)$$

$$\mathbf{ctx}_c^{(\ell)} := \frac{1}{T} \sum_t \mathbf{h}_{c,t}^{(\ell)} - \boldsymbol{\mu}^{(\ell)}. \quad (4)$$

Each of the four components has the following interpretations. For any given layer  $\ell$ ,

- we call  $\boldsymbol{\mu}^{(\ell)}$  the global mean vector, which differentiates neither contexts nor positions;
- we call  $(\mathbf{pos}_t^{(\ell)})_{t \leq T}$  the positional basis, as they quantify average positional effects;
- we call  $(\mathbf{ctx}_c^{(\ell)})_{c \leq C}$  the context basis, as they quantify average sequence/context effects;
- we call  $(\mathbf{resid}_{c,t}^{(\ell)})_{t \leq T, c \leq C}$  the residual vectors, which capture higher-order effects.
- In addition, we define  $\mathbf{cvec}_{c,t}^{(\ell)} = \mathbf{ctx}_c^{(\ell)} + \mathbf{resid}_{c,t}^{(\ell)}$ .

A corpus may contain billions of tokens. For practical use, in this paper  $C$  is much smaller: we subsample input sequences from the corpus; for example,  $C = 6.4K$  in Figure 1.

**Positional basis vs. positional embeddings.** While positional embeddings at Layer 0 is much explored in the literature (see Section 6), the structure in intermediate layers is poorly understood. In contrast, our approach offers structural insights to *all* layers.

## 1.2 Connections to ANOVA

Our embedding decomposition is similar to multivariate two-way ANOVA in form. Borrowing standard terminology from ANOVA, positions and contexts can be regarded as two *factors* or *treatments*, so viewing the embedding  $\mathbf{h}_{c,t}$  as the response variable, then positional/context bases represent mean effects.

**On terminology.** (i) We use *context* to refer to a sequence since its tokens collectively encode context information. (ii) We call positional/context basis for convenience. A more accurate term is *frame* or *over-complete basis*, since  $(\mathbf{pos}_t^{(\ell)})_{t \leq T}$  and  $(\mathbf{ctx}_c^{(\ell)})_{c \leq C}$  are often linearly dependent.

## 1.3 Accessible reproducibility

We provide a fast implementation via Google Colab that reproduces most of the figures and analysis for GPT-2 (under several minutes with the GPU option):

[https://colab.research.google.com/drive/1ubsJQvLkOSQtIU8LoBA\\_79t1bd5-5ihi?usp=sharing](https://colab.research.google.com/drive/1ubsJQvLkOSQtIU8LoBA_79t1bd5-5ihi?usp=sharing).

The complete implementation, as well as additional plots and measurements, can be found on the following GitHub page.

<https://github.com/JiajunSong629/uncover-hidden-geometry>

## 1.4 Notations

For a vector  $\mathbf{x}$ , we denote its  $\ell_2$  norm by  $\|\mathbf{x}\|$ . For a matrix  $\mathbf{A} \in \mathbb{R}^{n \times m}$ , we denote its operator norm by  $\|\mathbf{A}\|_{\text{op}} := \max_{\mathbf{u}: \|\mathbf{u}\|=1} \|\mathbf{A}\mathbf{u}\|$  and max norm by  $\|\mathbf{A}\|_{\text{max}} := \max_{i,j} |A_{ij}|$ . We use the standard big- $O$  notation: for positive scalars  $a, b$ , we write  $a = O(b)$  if  $a \leq Cb$  for a constant  $C$ . We use  $\text{span}(\mathbf{M})$  to denote the linear span of column vectors in  $\mathbf{M}$ .

Table 1: **Averaged (and std of) measurements across layers.** Measurements based on 6.4K samples. All values are in  $[0, 1]$  except ‘rank estimate’: ‘relative norm’ means magnitude of positional basis relative to centered embeddings; ‘similarity’ and ‘incoherence’ are averaged *cosine similarity* (inner products of normalized vectors) between **ctx**, and between **ctx** and **pos**, respectively. We find (i) positional basis is a **low-rank** and **significant** component (ii) inter similarity  $\ll$  intra similarity (iii) **incoherence** between two bases.

		Positional basis		Context basis		Incoherence
		rank estimate	relative norm	inter-cluster similarity	intra-cluster similarity	
NanoGPT	Shakespeare	7.86 (1.96)	0.66 (0.28)	——	——	——
GPT-2	OpenWebText	11.38 (1.86)	0.84 (0.18)	0.10 (0.01)	0.44 (0.04)	0.051 (0.05)
	WikiText	11.69 (1.64)	0.76 (0.18)	0.11 (0.01)	0.41 (0.03)	0.039 (0.04)
BERT	OpenWebText	12.54 (2.73)	0.78 (0.18)	0.13 (0.04)	0.26 (0.04)	0.046 (0.05)
	WikiText	12.62 (2.70)	0.76 (0.18)	0.17 (0.03)	0.31 (0.04)	0.043 (0.04)
BLOOM	OpenWebText	10.23 (1.31)	0.30 (0.16)	0.15 (0.14)	0.32 (0.09)	0.158 (0.23)
	WikiText	10.00 (1.47)	0.31 (0.13)	0.14 (0.13)	0.31 (0.09)	0.148 (0.23)
Llama 2	OpenWebText	9.38 (1.15)	0.14 (0.03)	0.17 (0.19)	0.43 (0.12)	0.190 (0.24)
	WikiText	8.69 (0.91)	0.07 (0.04)	0.47 (0.35)	0.60 (0.25)	0.316 (0.27)
	GitHub	8.69 (1.67)	0.21 (0.05)	0.17 (0.10)	0.40 (0.07)	0.189 (0.20)

## 2 Pervasive geometrical structure

We apply our decomposition to a variety of pretrained transformers including GPT-2 [Radford et al. \(2019\)](#), BERT [Devlin et al. \(2018\)](#), BLOOM [Scao et al. \(2022\)](#), Llama-2 [Touvron et al. \(2023\)](#), and various datasets such as WikiText, OpenWebText, GitHub. See Section A for details. Our geometric findings are summarized below.

1. Positional basis is a significant and approximately low-rank component, forming a continuous and curving shape.
2. Context basis has strong cluster patterns corresponding to documents/topics.
3. Positional basis and context basis are nearly orthogonal (or *incoherent*).

Our findings indicate that embeddings contain two main interpretable factors, which are decoupled due to incoherence.

**Sinusoidal patterns are learned, not predefined.** The transformers we examined are trained from scratch including the positional embeddings (PEs). It is unclear a priori why such a smooth and sinusoidal pattern is consistently observed. Moreover, the learned sinusoidal patterns are different from the original fixed sinusoidal embedding [Vaswani et al. \(2017\)](#): for example, the original PE is concentrated less on the low-frequency components (Section B.1).

**Consistent pattern across layers and models is not solely explained by residual connections.** The geometric structure is (i) consistent across layers and (ii) agnostic to models. Can consistency across layers explained by residual connections? We show this is not true: the average norm of embeddings increases by more than 100-fold in GPT-2, and the embeddings are nearly orthogonal between layer 0 and 1 (Section B.2).



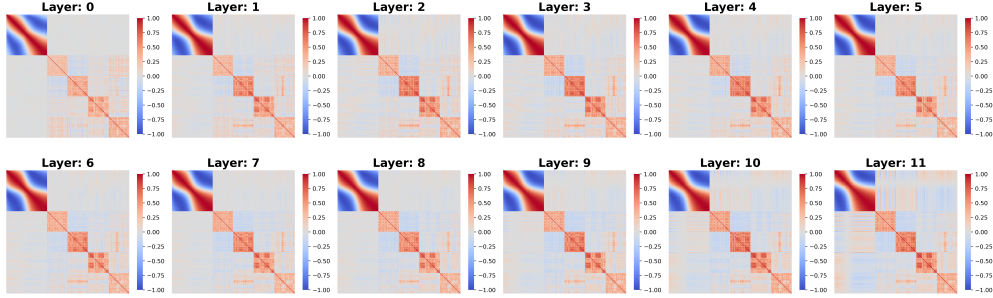


Figure 2: **Normalized Gram matrix**  $[\bar{P}, \bar{C}]^\top [\bar{P}, \bar{C}]$  where  $\bar{P} = [\frac{\text{pos}_1}{\|\text{pos}_1\|}, \dots, \frac{\text{pos}_T}{\|\text{pos}_T\|}]$  and  $\bar{C} = [\frac{\text{ctx}_1}{\|\text{ctx}_1\|}, \dots, \frac{\text{ctx}_C}{\|\text{ctx}_C\|}]$  based on GPT-2. Here,  $T = 128$ , and  $\text{ctx}_c$  is sampled from 4 documents with sample size 32 in OpenWebText. We find (i) **Smoothness**, pos-pos part (top left) of Gram matrix is smooth; (ii) **Incoherence**, pos-ctx part (top right/bottom left) has values close to 0; (iii) **Clustering**, ctx-ctx part (bottom right) shows strong cluster patterns.

**Some exceptions.** In the last few layers, embeddings tend to be anisotropic [Ethayarajh \(2019\)](#) and geometric structure may collapse to a lower dimensional space, particularly the positional basis. It is possibly due to the completion of contextualization or optimization artifacts. We also find that BERT shows higher frequency patterns, possibly due to its different training.

### 3 Key properties of positional basis: low rank and low frequency

In this section, we use quantitative measurements to relate smoothness to concepts in parsimonious representations.

**Measuring smoothness.** Our notion of “smoothness” of the positional basis refers to its (normalized) Gram matrix:

$$G = \bar{P}^\top \bar{P} \in \mathbb{R}^{T \times T}, \text{ where } \bar{P} = [\frac{\text{pos}_1}{\|\text{pos}_1\|}, \dots, \frac{\text{pos}_T}{\|\text{pos}_T\|}] \quad (5)$$

being visually smooth (mathematically, having bounded discrete derivatives).

#### 3.1 Low rank via spectral analysis

**Low rank.** We find that the positional basis concentrates around a low-dimensional subspace. In Table 1 “rank estimate” column, we report the rank estimate of positional basis averaged across all layers using the method of [Donoho et al. \(2023\)](#). In Figure 3, we plot the top singular values in descending order of  $P = [\text{pos}_1, \dots, \text{pos}_T]$ . Visibly, there is a sharp change in the plot, which indicate a dominant low-rank structure. In Section C.2, we report detailed rank estimates.

**Significant in relative norms.** We also find that usually, the positional basis accounts for a signifi-

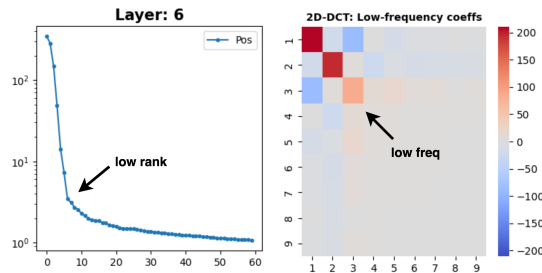


Figure 3: **Spectral and Fourier analysis** based on GPT-2 model and OpenWebText. **Left:** Top-60 singular values of  $P$ . **Right:** Applying 2D discrete cosine transform to  $\bar{P}^\top \bar{P}$ , we show first 10 frequency coefficients.

cant proportion of embeddings. In Table 1, we report the relative norm (averaged across layers)  $\|\mathbf{P}\|_{\text{op}}/\|\mathbf{M}\|_{\text{op}}$ , where  $\mathbf{M}$  contains centered embedding vectors  $\mathbf{h}_{c,t} - \boldsymbol{\mu}$  and columns of  $\mathbf{P}$  are corresponding  $\text{pos}_t$ . The relative norms show positional basis is contributing significantly to the overall magnitude (most numbers bigger than 10%).

### 3.2 Low frequency via Fourier analysis

In Figure 3 (right), we apply the 2D discrete cosine transform to the normalized Gram matrix  $\bar{\mathbf{P}}^\top \bar{\mathbf{P}}$ ; namely, we calculate the frequency matrix  $\hat{\mathbf{G}}$  by apply the (type-II) discrete cosine transform with orthogonal matrix  $\tilde{\mathbf{F}}$ :

$$\hat{\mathbf{G}} = \tilde{\mathbf{F}} \mathbf{G} \tilde{\mathbf{F}}^\top.$$

Each entry  $\hat{G}_{ij}$  encodes the  $(i, j)$ -th frequency coefficient. We discover that energies are concentrated mostly in the low-frequency components, which echos the smooth and curving structure in Figure 1.

### 3.3 Theoretical lens: smoothness explains low-rank and low-frequency

It is well known that the smoothness of a function is connected to fast decay or sparsity in the frequency domain (Pinsky, 2008, Sect. 1.2.3). From the classical perspective, we establish smoothness as a critical property that induces the observed geometry.

*Smoothness of Gram matrix of positional basis induces the low-dimensional and spiral shape.*

For convenience, we assume that positional vectors  $\text{pos}_t$  have unit norm, so by definition,  $\text{pos}_1 + \dots + \text{pos}_T = \mathbf{0}$ . To quantify smoothness, we introduce the definition of finite difference. As with the discrete cosine transform in 1D, we extend and reflect the Gram matrix to avoid boundary effects.

Let  $\mathbf{G}^{(1)} = \mathbf{G}$  and  $\mathbf{G}^{(2)}, \mathbf{G}^{(3)}, \mathbf{G}^{(4)} \in \mathbb{R}^{T \times T}$  be defined by  $\mathbf{G}_{t,t'}^{(2)} = \mathbf{G}_{t,T+1-t',}$   $\mathbf{G}_{t,t'}^{(3)} = \mathbf{G}_{T+1-t,t'},$   $\mathbf{G}_{t,t'}^{(4)} = \mathbf{G}_{T+1-t,T+1-t'}$  for any  $t, t' = 1, 2, \dots, T$ . We extend and reflect  $\mathbf{G}$  by

$$\tilde{\mathbf{G}} := \begin{pmatrix} \mathbf{G}^{(1)} & \mathbf{G}^{(2)} \\ \mathbf{G}^{(3)} & \mathbf{G}^{(4)} \end{pmatrix}. \quad (6)$$

We define the first-order finite difference by (using periodic extension  $\tilde{G}_{t \pm 2T, t' \pm 2T} = \tilde{G}_{t, t'}$ )

$$[\Delta^{(1,1)} \tilde{\mathbf{G}}]_{t,t'} = T^2 (\tilde{G}_{t,t'} - \tilde{G}_{t-1,t'} - \tilde{G}_{t,t'-1} + \tilde{G}_{t-1,t'-1}) \quad (7)$$

for all integers  $t, t'$ . Higher-order finite differences are defined recursively by  $\Delta^{(m,m)} \tilde{\mathbf{G}} = \Delta^{(1,1)} (\Delta^{(m-1,m-1)} \tilde{\mathbf{G}})$ .

Note that  $\Delta^{(m,m)} \tilde{\mathbf{G}}$  measures higher-order smoothness of  $\tilde{\mathbf{G}}$ . Indeed, if  $G_{t,t'} = f(t/T, t'/T)$  for certain smooth function  $f(x, y)$  defined on  $[0, 1]^2$ , then  $[\Delta^{(m,m)} \tilde{\mathbf{G}}]_{t,t'} \approx \partial_x^m \partial_y^m f(t/T, t'/T)$ .

**Theorem 1.** Fix positive integers  $k \leq T$  and  $m$ . Define the low-frequency vector  $\mathbf{f}_s = (1, \cos((s - 0.5)\pi/T), \dots, \cos((s - 0.5)(T - 1)\pi/T))^\top \in \mathbb{R}^T$  where  $s = 1, \dots, k$ , and denote  $\mathbf{F}_{\leq k} = [\mathbf{f}_1, \dots, \mathbf{f}_k] \in \mathbb{R}^{T \times k}$ . Then there exists  $\mathbf{B} \in \mathbb{R}^{k \times k}$  such that

$$\frac{1}{T} \left\| \mathbf{G} - \mathbf{F}_{\leq k} \mathbf{B} (\mathbf{F}_{\leq k} \mathbf{B})^\top \right\|_{\text{op}} \leq \frac{6}{(8k)^m} \|\Delta^{(m,m)} \tilde{\mathbf{G}}\|_{\max}.$$

This theorem implies that if the extended Gram matrix has higher-order smoothness, namely  $\|\Delta^{(m,m)} \tilde{\mathbf{G}}\|_{\max}$  is bounded by a constant, then even for moderate  $k$  and  $m$ , we have approximation  $\mathbf{G} \approx \mathbf{F}_{\leq k} \mathbf{B} (\mathbf{F}_{\leq k} \mathbf{B})^\top$ . Note that  $\mathbf{F}_{\leq k} \mathbf{B}$  consists of linear combinations of low-frequency vectors. This explains why  $\mathbf{G}$  has a dominant low-rank and low-frequency component.

Table 2: **Robustness of positional basis.** Similar geometric structures found on *OOD* samples: NanoGPT (trained on a Shakespeare dataset) evaluated on WikiText, GPT-2 and BERT (trained on language datasets) evaluated on GitHub data, BLOOM evaluated on random tokens.

	rank estimate of $\mathbf{P}$	ratio explained by low-freq ( $K = 10$ )
NanoGPT	5.43 (1.84)	84.0%
GPT-2	11.54 (1.55)	99.5%
BERT	12.46 (2.47)	70.2%
BLOOM	10.44 (2.25)	95.6%

Table 3: **Inheriting smoothness from positional basis.** For  $K = 1, 3, 5, 10$ , we apply 2D DCT and calculate the ratio<sup>1</sup> of up to  $K$ -th low-frequency coefficients based on GPT-2 and positional basis.

Ratio explained	$K = 1$	$K = 3$	$K = 5$	$K = 10$
$\mathbf{P}\mathbf{P}^\top$	39.4%	95.4%	98.2%	99.7%
$\mathbf{P}\mathbf{W}\mathbf{P}^\top$	45.9%	96.5%	98.8%	99.9%
QK matrix	84.0%	90.0%	90.4%	91.2%

## 4 Smoothness: blessing of natural languages

We demonstrate that smoothness is a natural and beneficial property learned from language data: it is robust to distribution shifts and allows efficient attention computation. This smoothness likely reflects the nature of language data.

### 4.1 Smoothness is robust in out-of-distribution data

So far, we have analyzed our decomposition and associated geometry primarily on *in-distribution* samples. For example, we sample sequences from OpenWebText—the same corpus GPT-2 is pretrained on, to calculate decomposition (3)–(4).

Now we sample out-of-distribution (OOD) data and conduct similar decomposition and analyses. We find that the positional basis possesses similar low-rank and spiral structure. Surprisingly, for sequences consisting of randomly sampled tokens, such structure persists. See summaries in Table 2 and details in Section D.1.

Many LLMs can generalize well to OOD data. We believe that this generalization ability is at least partially attributed to the robustness of positional basis as evidenced here.

### 4.2 Smoothness promotes local and sparse attention

Many attention heads in large-scale transformers for language data show local and sparse patterns (Beltagy et al., 2020). A usual heuristic explanation is that, most information for token prediction is contained in a local window.

We offer an alternative explanation: *Local attention is a consequence of smoothness of positional basis.*

We provide our reasoning. First, in terms of smoothness, the Gram matrix  $\mathbf{P}\mathbf{P}^\top$  is closely related to  $\mathbf{P}\mathbf{W}\mathbf{P}^\top$ , where  $\mathbf{W} = \mathbf{W}^q(\mathbf{W}^k)^\top / \sqrt{d_{\text{head}}}$ . Indeed, generally a linear transformation of the positional vectors, namely  $\mathbf{W}\mathbf{P}^\top$ , should not affect smoothness much.

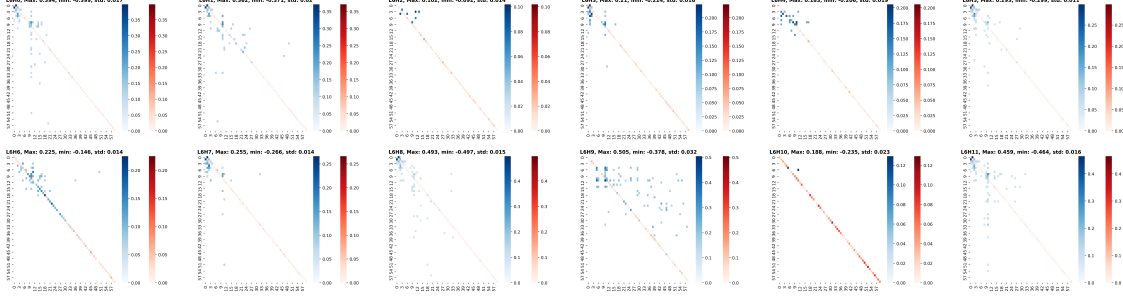


Figure 4: **Decoupling trained weight matrices.** For 12 attention heads (layer  $L = 6$  shown here) in GPT-2, we study the matrix  $\mathbf{W} = \mathbf{W}^q(\mathbf{W}^k)^\top / \sqrt{d_{\text{head}}} \in \mathbb{R}^{d \times d}$ . **Red:** diagonal entries  $\mathbf{D} := \text{diag}(\mathbf{W})$ . **Blue:** take off-diagonal matrix  $\mathbf{W} - \text{diag}(\mathbf{W})$ , rotate it by the right singular vectors of positional basis  $\mathbf{V}$ , then apply denoising. Large absolute values concentrate in small top-left part  $\mathbf{L}$ .

Second,  $\mathbf{P}\mathbf{W}\mathbf{P}^\top$  is an important—often dominant—constituent of the QK matrix (QK matrix is the matrix inside softmax in (1)); see Section 5.2 for an example. Thus, the QK matrix can inherit the smoothness from  $\mathbf{P}\mathbf{W}\mathbf{P}^\top$ .

Third, if the QK matrix (denoted by  $\mathbf{B}$ ) is smooth and maximized at the diagonal position along a certain row indexed by  $t$  (the constraint  $t' \leq t$  is due to causal masking):

$$\arg \max_{1 \leq t' \leq t} B_{t,t'} = t, \quad (8)$$

then positions  $t'$  close to  $t$  also have high QK values by smoothness. Therefore, we expect the neighboring positions around  $t$  to receive high attention weights after softmax.

Our reasoning is supported by pervasive smoothness shown in Table 3. Moreover, we find that the positional constituents in more than 43% heads in GPT-2 satisfy (8) for more than 80% positions  $t$ . See Section D.2 for details.

### 4.3 Curse of discontinuity for arithmetic tasks

We find that the emergence of smoothness is data dependent: while transformers pretrained on natural/programming languages exhibit the smoothness property, they may suffer from a lack of smoothness on other pretrained data.

We explore a simple arithmetic task—*Addition*, where inputs are formatted as a string “ $a + b = c$ ” with  $a, b, c$  represented by digits of a certain length. We sample the length of each addition component uniformly from  $\{L/2, \dots, L\}$  where  $L = 10$ . Then, we train a 4-layer 4-head transformer (NanoGPT) with character-level tokenization to predict ‘ $c$ ’ based on the prompt “ $a + b =$ ”. We train this transformer 10,000 iterations until convergence.

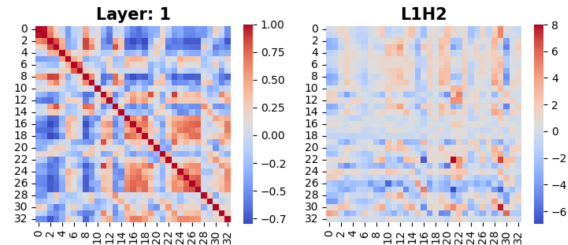


Figure 5: Addition task trained on NanoGPT exhibits **nonsmooth** patterns: **discontinuity** as a consequence of non-language data training. **Left:** Gram matrix of normalized positional basis. Compare with top-left of plots in Figure 2. **Right:** QK matrix.

<sup>1</sup>Given 2D frequencies  $(f_{ij})$ , we calculate the ratio as  $r_K = \sum_{i,j \leq K} f_{ij}^2 / \sum_{i,j} f_{ij}^2$ .

**Nonsmooth pattern.** Figure 5 shows that the Gram matrix of normalized positional basis and QK matrix are visibly discontinuous and exhibit many fractured regions. Quantitatively, the top-10 low-frequency components of Gram matrix explains around 50% of  $\sum_{ij} \hat{G}_{ij}^2$  (Section D.3), much less than 99% in GPT-2 as in Table 3. This suggests a sharp distinction between language vs. non-language data in terms of induced geometry.

**Failure of length generalization.** Our NanoGPT achieves above 99% in-distribution test accuracy, yet fails at OOD generalization: it has less than 20% accuracy on average on digits of length smaller than 5. We believe nonsmoothness is likely an intrinsic bottleneck for arithmetic tasks.

Our results hold for transformers with relative positional embeddings as well; see Section D.3.

## 5 Incoherence enhances interpretability

Near-orthogonality, or (mutual) incoherence, is known to be a critical property for sparse learning. Generally speaking, incoherence means that factors or features are nearly uncorrelated and decoupled. In the ideal scenario of orthogonality, factors can be decomposed into orthogonal non-intervening subspaces. Incoherence is closely related to *restricted isometry* (Candes & Tao, 2005), *irrepresentable conditions* (Zhao & Yu, 2006), etc.

We observe the incoherence property between the positional basis and the context basis, as Table 1 shows that  $\max_{t,c} |\langle \frac{\mathbf{pos}_t}{\|\mathbf{pos}_t\|}, \frac{\mathbf{ctx}_c}{\|\mathbf{ctx}_c\|} \rangle|$  is typically small. The low incoherence in Table 1 (random baseline is about 0.1) means that the two bases are nearly orthogonal to each other.

To decouple different effects, in this section, we will focus on positional effects vs. non-positional effects, thus working with  $\mathbf{cvec}_{c,t}$  instead of  $\mathbf{ctx}_c$ .

### 5.1 Decoupling positional effects in pretrained weights

We present evidence that the trained weight matrix  $\mathbf{W} := \mathbf{W}^q (\mathbf{W}^k)^\top / \sqrt{d_{\text{head}}}$  in self-attention has a clear and interpretable decomposition: heuristically, a low rank component that modulates the positional effects, and a diagonal component that strengthens or attenuates token effects.

More precisely, we identify a common *low-rank plus noise* structure in the majority of attention heads in pretrained transformers.

$$\mathbf{W} = \underbrace{\mathbf{V}\mathbf{L}\mathbf{V}^\top}_{\text{low rank}} + \underbrace{\mathbf{D}}_{\text{diagonal}} + \text{Noise} . \quad (9)$$

Here, the columns of  $\mathbf{V} \in \mathbb{R}^{d \times K}$  are the top- $K$  right singular vectors of positional basis matrix  $\mathbf{P}$ , and  $\mathbf{L} \in \mathbb{R}^{K \times K}$ , where  $K$  is not large.

Figure 4 shows empirical support to structural claim (9). Given a pretrained weight  $\mathbf{W}$ , we take  $\mathbf{D} = \text{diag}(\mathbf{W})$  and show entries in red. Then, we rotate the off-diagonal part of  $\mathbf{W}$  by the right singular vectors of  $\mathbf{P}$  and apply denoising, namely zeroing entries whose absolute values are smaller than a threshold. For many heads, the surviving large absolute values are concentrated in the top left ( $K \approx 20$ )—which suggests that indeed a significant component of  $\mathbf{W}$  is aligned with the positional basis.

This decomposition suggests a possible mechanism inside attention computation. Consider an ideal scenario where  $\mathbf{D}$  is a multiple of identity matrix, and each embedding has orthogonal decomposition  $\mathbf{h} = \mathbf{t} + \mathbf{c}$  with  $\mathbf{t} \in \text{span}(\mathbf{V})$  encoding positional information and  $\mathbf{c} \in \text{span}(\mathbf{V})^\perp$  encoding non-positional information. Then, for two embedding vectors  $\mathbf{h}, \mathbf{h}'$  with  $\mathbf{h} = \mathbf{t} + \mathbf{c}$  and  $\mathbf{h}' = \mathbf{t}' + \mathbf{c}'$ ,

$$\mathbf{h}^\top \mathbf{W} \mathbf{h}' \approx \underbrace{\mathbf{t}^\top (\mathbf{V}\mathbf{L}\mathbf{V}^\top + \mathbf{D}) \mathbf{t}'}_{\text{positional effect}} + \underbrace{\mathbf{c}^\top \mathbf{D} \mathbf{c}'}_{\text{context / token effect}}$$

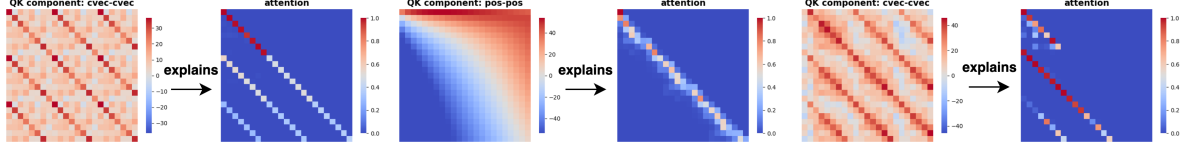


Figure 6: **QK constituent plots enhance attention visualization:** 3 representative attention patterns in induction heads can be explained by their respective dominant QK constituents. **Left pair:** *cvec-cvec* constituent drives attention to identical tokens. **Middle pair:** *pos-pos* constituent determines attention to neighboring tokens. **Right pair:** *cvec-cvec* shows attentions to shifted tokens.

Positional effects are decoupled from context effects, since cross terms involving  $t, c'$  or  $t', c$  vanish. This heuristics may allow us to examine how information is processed in attention heads, which will be explored in future work.

## 5.2 Beyond attention visualization

Attention visualization is often used as a diagnosis of self-attention in transformers. We show that more structure can be revealed by decomposing the QK matrix using our decomposition of embeddings.

We start with decomposing the QK matrix. Assuming  $\mu = \mathbf{0}$  (ignoring global mean effect for convenience), then for embedding vectors  $h, h' \in \mathbb{R}^d$  we have

$$\begin{aligned} h^\top W^q (W^k)^\top h &= \text{pos}^\top W^q (W^k)^\top \text{pos} \\ &+ \text{pos}^\top W^q (W^k)^\top \text{cvec} + \text{cvec}^\top W^q (W^k)^\top \text{pos} \\ &+ \text{cvec}^\top W^q (W^k)^\top \text{cvec}. \end{aligned} \quad (10)$$

Each of the four components shows how much an attention head captures information from cross-pairs *pos/cvec*—*pos/cvec* of an embedding. We propose to visualize each QK component separately, which tells if an attention head captures positional information or context/token information from embeddings.

**Case study: induction heads.** Elhage et al. (2021) identified components in transformers that complete a sequence pattern based on observed past tokens, namely, predicting the next token  $[B]$  based on observed sequence  $[A], [B], \dots, [A]$ . This ability of copying previous tokens is known to be caused by *induction heads*.

There are three representative attention patterns as shown in Figure 6: (i) attention to identical tokens, namely attention weights concentrate on tokens identical to the present token, (ii) attention to neighboring tokens, (iii) attention to tokens to be copied. See also Elhage et al. (2021).

Attention visualization alone does not reveal why certain heads emerge. In contrast, our QK decomposition reveals which QK constituent is dominant and responsible for attention patterns. For example, in Figure 6,

- attention to neighboring tokens (middle plots) is predominately determined by the **pos-pos** constituent;
- attention to identical token (left) or shifted token (right) is determined by the **cvec-cvec** constituent. This implies that induction heads are not based on memorizing relative positions, but on matching token information.

More details are in Section E.2.



### 5.3 Theoretical insight from kernel factorization

Why does incoherence emerge from pretrained transformers? While it is well known in sparse coding and compressed sensing that *handcrafted* incoherent basis facilitates recovery of sparse signals (Donoho & Stark, 1989; Donoho & Elad, 2003; Donoho, 2006; Candès et al., 2006), it is surprising that incoherence arises from *automatic feature learning*.

Here we focus on the self-attention mechanism of transformers. By adopting the kernel perspective, we present a preliminary theory for the following heuristics:

*Incoherence enables a kernel to factorize into smaller components, each operating independently.*

Given query/key matrices  $\mathbf{W}^q, \mathbf{W}^k \in \mathbb{R}^{d \times d_{\text{head}}}$ , we define the (asymmetric) kernel by (recalling  $\mathbf{W} = \mathbf{W}^q(\mathbf{W}^k)^\top / \sqrt{d_{\text{head}}}$ )

$$K_{\mathbf{W}}(\mathbf{z}, \mathbf{z}') := \exp(\mathbf{z}^\top \mathbf{W} \mathbf{z}') = \exp\left(\frac{\langle \mathbf{W}^q \mathbf{z}, \mathbf{W}^k \mathbf{z}' \rangle}{\sqrt{d_{\text{head}}}}\right).$$

Using  $K_{\mathbf{W}}$ , the attention can be expressed as kernel smoothing: for embeddings  $(\mathbf{x}_t)_{t \leq T} \subset \mathbb{R}^d$ ,

$$\text{AttnHead}(\mathbf{x}_t; K_{\mathbf{W}}) = \sum_{k \leq t} \frac{K_{\mathbf{W}}(\mathbf{x}_k, \mathbf{x}_t)}{\sum_{k' \leq t} K_{\mathbf{W}}(\mathbf{x}_{k'}, \mathbf{x}_t)} v(\mathbf{x}_k) \quad (11)$$

where  $v : \mathbb{R}^d \rightarrow \mathbb{R}$  is a generic value function. This kernel perspective is explored in Tsai et al. (2019), where it is argued that the efficacy of self-attention largely depends on the form of the kernel.

Suppose that there are two overcomplete bases  $\mathcal{B}_1^0, \mathcal{B}_2^0 \subset \mathbb{R}^d$ . For simplicity, assume that  $\|\mathbf{u}\|_2 \leq 1$  if  $\mathbf{u} \in \mathcal{B}_1^0$  or  $\mathcal{B}_2^0$ . The mutual incoherence is  $\text{incoh} := \max \{|\langle \mathbf{c}, \mathbf{t} \rangle| : \mathbf{c} \in \mathcal{B}_1^0, \mathbf{t} \in \mathcal{B}_2^0\}$ . Consider the (extended) overcomplete basis  $\mathcal{B}_\alpha := \{\lambda \mathbf{u} : \mathbf{u} \in \mathcal{B}_\alpha^0, \lambda \in [-1, 1]\}$  where  $\alpha \in \{1, 2\}$ . Given query/key vectors  $\mathbf{x}^q, \mathbf{x}^k \in \mathbb{R}^d$ , suppose that we can decompose them according to the two bases.

$$\mathbf{x}^q = \mathbf{c}^q + \mathbf{t}^q, \quad \mathbf{x}^k = \mathbf{c}^k + \mathbf{t}^k, \quad \text{for } \mathbf{c}^q, \mathbf{c}^k \in \mathcal{B}_1; \mathbf{t}^q, \mathbf{t}^k \in \mathcal{B}_2. \quad (12)$$

Generically, we can decompose  $K_{\mathbf{W}}(\mathbf{x}^q, \mathbf{x}^k)$  into

$$K_{\mathbf{W}}(\mathbf{c}^q, \mathbf{c}^k) K_{\mathbf{W}}(\mathbf{c}^q, \mathbf{t}^k) \cdot K_{\mathbf{W}}(\mathbf{t}^q, \mathbf{c}^k) K_{\mathbf{W}}(\mathbf{t}^q, \mathbf{t}^k).$$

Each component measures cross similarity of pairs between  $\mathbf{c}^q, \mathbf{t}^q$  and  $\mathbf{c}^k, \mathbf{t}^k$ , which then translates into a weight for the attention. Unfortunately, this general decomposition requires the individual kernels to share the same weight  $\mathbf{W}$ , which hinders capturing cross interactions flexibly.

It turns out that if the weight matrix is *sparsely represented* by the bases, then kernel flexibility can be achieved. To be precise, we will say that  $\mathbf{W} \in \mathbb{R}^{d \times d}$  is  $s$ -sparsely represented by bases  $\mathcal{B}, \mathcal{B}'$  if there exist  $(a_k)_{k \leq s} \subset [-1, 1]$ ,  $(\mathbf{u}_k)_{k \leq s} \subset \mathcal{B}$ ,  $(\mathbf{v}_k)_{k \leq s} \subset \mathcal{B}'$  such that

$$\mathbf{W} = \sum_{k \leq s} a_k \mathbf{u}_k \mathbf{v}_k^\top. \quad (13)$$

**Theorem 2.** Let  $\mathbf{W}_{11}, \mathbf{W}_{12}, \mathbf{W}_{21}, \mathbf{W}_{22} \in \mathbb{R}^{d \times d}$  be any matrices with the following properties: for  $\alpha, \beta \in \{1, 2\}$ ,  $\mathbf{W}_{\alpha\beta} \in \mathbb{R}^{d \times d}$  is  $O(1)$ -sparsely represented by bases  $\mathcal{B}_\alpha, \mathcal{B}_\beta$ . Then for all  $\mathbf{x}^q, \mathbf{x}^k \in \mathbb{R}^d$  satisfying (12),  $\mathbf{W} = \mathbf{W}_{11} + \mathbf{W}_{12} + \mathbf{W}_{21} + \mathbf{W}_{22}$  satisfies

$$K_{\mathbf{W}}(\mathbf{x}^q, \mathbf{x}^k) = (1 + O(\text{incoh})) \cdot K_{\mathbf{W}_{11}}(\mathbf{c}^q, \mathbf{c}^k) K_{\mathbf{W}_{12}}(\mathbf{c}^q, \mathbf{t}^k) \cdot K_{\mathbf{W}_{21}}(\mathbf{t}^q, \mathbf{c}^k) K_{\mathbf{W}_{22}}(\mathbf{t}^q, \mathbf{t}^k) \quad (14)$$



Moreover, (14) holds with probability at least  $1 - O(|\mathcal{B}_1^0| \cdot |\mathcal{B}_2^0|) \exp(-\text{incoh}^2 \cdot d)$  if each  $\mathbf{W}_{\alpha\beta}$  is replaced by  $\mathbf{W}_{\alpha\beta} + \frac{\mathbf{Z}_{\alpha\beta}}{\sqrt{d}}$  where  $(\mathbf{Z}_{\alpha\beta})_{kk'}$  is an independent subgaussian<sup>2</sup> random variable.

The factorization (14) says that each kernel component has a separate weight matrix, and all components contribute multiplicatively to  $K_{\mathbf{W}}$ . The “moreover” part generalizes the sparse representation notion by allowing additive noise, which matches the empirical structure in (9). The additive construction of  $\mathbf{W}$  is connected to *task arithmetic* (Ilharco et al., 2022; Ortiz-Jimenez et al., 2023) recently studied.

**Remark 1.** If we suppose  $\text{incoh} \asymp d^{-\gamma}$  with  $1/2 > \gamma > 0$ , then the high probability statement is nontrivial if  $|\mathcal{B}_1^0| \cdot |\mathcal{B}_2^0| = o(\exp(d^{1-2\gamma}))$ . This dictionary size limit is generally reasonable.

## 6 Related work

Analyses of transformers have attracted research interest since Vaswani et al. (2017). Many studies on GPT-2 (Radford et al., 2019) and BERT (Devlin et al., 2018) show that last-layer contextualized embeddings capture linguistic structure and exhibit excellent downstream performance (Hewitt & Manning, 2019; Chi et al., 2020; Thompson & Mimno, 2020). Fewer papers focus on the geometry or intermediate-layer embeddings: in Ethayarajh (2019), it is found that later-layer embeddings are increasingly anisotropic and context-specific; Cai et al. (2020); Reif et al. (2019); Hernandez & Andreas (2021); Gao et al. (2019) observed interesting geometric structures and artifacts without thorough analysis; Yeh et al. (2023) provide visualization tools for embeddings. Very recent papers provide empirical/theoretical evidence about either low-rank or diagonal structure in attention weight matrices (Boix-Adsera et al., 2023; Trockman & Kolter, 2023). Our decomposition unifies scattered empirical phenomena, reveals consistent geometry and explains observed artifacts (anisotropic, spiral shape, etc.).

Many variants of positional embedding are proposed (Shaw et al., 2018; Dai et al., 2019; Su et al., 2021; Scao et al., 2022; Press et al., 2021) since Vaswani et al. (2017). Since GPT-4, many papers focus on length generalization for arithmetic tasks (Kazemnejad et al., 2023; Lee et al., 2023). Prior analyses on positional embeddings focus only on static (0-th layer) embeddings for selected transformers (Wang et al., 2020; Ke et al., 2020; Wang & Chen, 2020; Tsai et al., 2019; Yamamoto & Matsuzaki, 2023), whereas we provide a more detailed picture.

Prior work on LSTMs finds decomposition-based methods enhance interpretability (Murdoch et al., 2018). Understanding the inner workings of transformers is usually done through attention visualization (Clark et al., 2019; Wang et al., 2022). The emergence of induction heads (Elhage et al., 2021; Olsson et al., 2022) is supported by attention visualization, which is further reinforced by our analysis.

## 7 Limitations

In this paper, we mostly focus on pretrained transformers due to limited computational resources. It would be interesting to investigate the impact of input/prompt formats on the geometry of embeddings over the course of training, especially for different linguistic tasks and arithmetic tasks.

Also, we mostly focus on the mean vectors  $\text{pos}_t$  and  $\text{ctx}_c$  but not study  $\text{resid}_{c,t}$  thoroughly. We find that the residual component is not negligible (e.g., containing token-specific information). It would be interesting to study the higher-order interaction in  $\text{resid}_{c,t}$  and propose a nonlinear decomposition of embeddings, which is left to future work.

<sup>2</sup>We say that a random variable  $\xi$  is subgaussian if  $\mathbb{E}[\xi] = 0$  and  $\mathbb{E}[\exp(\lambda\xi)] \leq \exp(\lambda^2/2)$  for all  $\lambda \in \mathbb{R}$ .

## **8 Acknowledgement**

We thank Junjie Hu, Tim Ossowski, Harmon Bhasin, Wei Wang for helpful discussions.

Support for this research was provided by the Office of the Vice Chancellor for Research and Graduate Education at the University of Wisconsin–Madison with funding from the Wisconsin Alumni Research Foundation.

## References

- Beltagy, I., Peters, M. E., and Cohan, A. Longformer: The long-document transformer. *arXiv preprint arXiv:2004.05150*, 2020.
- Boix-Adsera, E., Littwin, E., Abbe, E., Bengio, S., and Susskind, J. Transformers learn through gradual rank increase. *arXiv preprint arXiv:2306.07042*, 2023.
- Bommasani, R., Hudson, D. A., Adeli, E., Altman, R., Arora, S., von Arx, S., Bernstein, M. S., Bohg, J., Bosselut, A., Brunskill, E., et al. On the opportunities and risks of foundation models. *arXiv preprint arXiv:2108.07258*, 2021.
- Broughton, S. A. and Bryan, K. *Discrete Fourier analysis and wavelets: applications to signal and image processing*. John Wiley & Sons, 2018.
- Brown, T., Mann, B., Ryder, N., Subbiah, M., Kaplan, J. D., Dhariwal, P., Neelakantan, A., Shyam, P., Sastry, G., Askell, A., et al. Language models are few-shot learners. *Advances in neural information processing systems*, 33:1877–1901, 2020.
- Bubeck, S., Chandrasekaran, V., Eldan, R., Gehrke, J., Horvitz, E., Kamar, E., Lee, P., Lee, Y. T., Li, Y., Lundberg, S., et al. Sparks of artificial general intelligence: Early experiments with gpt-4. *arXiv preprint arXiv:2303.12712*, 2023.
- Cai, X., Huang, J., Bian, Y., and Church, K. Isotropy in the contextual embedding space: Clusters and manifolds. In *International Conference on Learning Representations*, 2020.
- Candes, E. J. and Tao, T. Decoding by linear programming. *IEEE transactions on information theory*, 51(12):4203–4215, 2005.
- Candès, E. J., Romberg, J., and Tao, T. Robust uncertainty principles: Exact signal reconstruction from highly incomplete frequency information. *IEEE Transactions on information theory*, 52(2):489–509, 2006.
- Chi, E. A., Hewitt, J., and Manning, C. D. Finding universal grammatical relations in multilingual bert. *arXiv preprint arXiv:2005.04511*, 2020.
- Clark, K., Khandelwal, U., Levy, O., and Manning, C. D. What does bert look at? an analysis of bert’s attention. *arXiv preprint arXiv:1906.04341*, 2019.
- Dai, Z., Yang, Z., Yang, Y., Carbonell, J., Le, Q. V., and Salakhutdinov, R. Transformer-xl: Attentive language models beyond a fixed-length context. *arXiv preprint arXiv:1901.02860*, 2019.
- Devlin, J., Chang, M.-W., Lee, K., and Toutanova, K. Bert: Pre-training of deep bidirectional transformers for language understanding. *arXiv preprint arXiv:1810.04805*, 2018.
- Donoho, D., Gavish, M., and Romanov, E. Screenot: Exact mse-optimal singular value thresholding in correlated noise. *The Annals of Statistics*, 51(1):122–148, 2023.
- Donoho, D. L. Compressed sensing. *IEEE Transactions on information theory*, 52(4):1289–1306, 2006.
- Donoho, D. L. and Elad, M. Optimally sparse representation in general (nonorthogonal) dictionaries via  $\ell^1$  minimization. *Proceedings of the National Academy of Sciences*, 100(5):2197–2202, 2003.

- Donoho, D. L. and Stark, P. B. Uncertainty principles and signal recovery. *SIAM Journal on Applied Mathematics*, 49(3):906–931, 1989.
- Elhage, N., Nanda, N., Olsson, C., Henighan, T., Joseph, N., Mann, B., Askell, A., Bai, Y., Chen, A., Conerly, T., DasSarma, N., Drain, D., Ganguli, D., Hatfield-Dodds, Z., Hernandez, D., Jones, A., Kernion, J., Lovitt, L., Ndousse, K., Amodei, D., Brown, T., Clark, J., Kaplan, J., McCandlish, S., and Olah, C. A mathematical framework for transformer circuits. *Transformer Circuits Thread*, 2021. <https://transformer-circuits.pub/2021/framework/index.html>.
- Ethayarajh, K. How contextual are contextualized word representations? comparing the geometry of bert, elmo, and gpt-2 embeddings. *arXiv preprint arXiv:1909.00512*, 2019.
- Gao, J., He, D., Tan, X., Qin, T., Wang, L., and Liu, T.-Y. Representation degeneration problem in training natural language generation models. *arXiv preprint arXiv:1907.12009*, 2019.
- Hernandez, E. and Andreas, J. The low-dimensional linear geometry of contextualized word representations. *arXiv preprint arXiv:2105.07109*, 2021.
- Hewitt, J. and Manning, C. D. A structural probe for finding syntax in word representations. In *Proceedings of the 2019 Conference of the North American Chapter of the Association for Computational Linguistics: Human Language Technologies, Volume 1 (Long and Short Papers)*, pp. 4129–4138, 2019.
- Ilharco, G., Ribeiro, M. T., Wortsman, M., Gururangan, S., Schmidt, L., Hajishirzi, H., and Farhadi, A. Editing models with task arithmetic. *arXiv preprint arXiv:2212.04089*, 2022.
- Kazemnejad, A., Padhi, I., Ramamurthy, K. N., Das, P., and Reddy, S. The impact of positional encoding on length generalization in transformers. *arXiv preprint arXiv:2305.19466*, 2023.
- Ke, G., He, D., and Liu, T.-Y. Rethinking positional encoding in language pre-training. *arXiv preprint arXiv:2006.15595*, 2020.
- Lee, N., Sreenivasan, K., Lee, J. D., Lee, K., and Papailiopoulos, D. Teaching arithmetic to small transformers. *arXiv preprint arXiv:2307.03381*, 2023.
- Murdoch, W. J., Liu, P. J., and Yu, B. Beyond word importance: Contextual decomposition to extract interactions from lstms. *arXiv preprint arXiv:1801.05453*, 2018.
- Olsson, C., Elhage, N., Nanda, N., Joseph, N., DasSarma, N., Henighan, T., Mann, B., Askell, A., Bai, Y., Chen, A., Conerly, T., Drain, D., Ganguli, D., Hatfield-Dodds, Z., Hernandez, D., Johnston, S., Jones, A., Kernion, J., Lovitt, L., Ndousse, K., Amodei, D., Brown, T., Clark, J., Kaplan, J., McCandlish, S., and Olah, C. In-context learning and induction heads. *Transformer Circuits Thread*, 2022. <https://transformer-circuits.pub/2022/in-context-learning-and-induction-heads/index.html>.
- Ortiz-Jimenez, G., Favero, A., and Frossard, P. Task arithmetic in the tangent space: Improved editing of pre-trained models. *arXiv preprint arXiv:2305.12827*, 2023.
- Pinsky, M. A. *Introduction to Fourier analysis and wavelets*, volume 102. American Mathematical Soc., 2008.
- Press, O., Smith, N. A., and Lewis, M. Train short, test long: Attention with linear biases enables input length extrapolation. *arXiv preprint arXiv:2108.12409*, 2021.
- Radford, A., Wu, J., Child, R., Luan, D., Amodei, D., Sutskever, I., et al. Language models are unsupervised multitask learners. *OpenAI blog*, 1(8):9, 2019.

- Reif, E., Yuan, A., Wattenberg, M., Viegas, F. B., Coenen, A., Pearce, A., and Kim, B. Visualizing and measuring the geometry of bert. *Advances in Neural Information Processing Systems*, 32, 2019.
- Rudelson, M. and Vershynin, R. Sampling from large matrices: An approach through geometric functional analysis. *Journal of the ACM (JACM)*, 54(4):21–es, 2007.
- Scao, T. L., Fan, A., Akiki, C., Pavlick, E., Ilić, S., Hesslow, D., Castagné, R., Luccioni, A. S., Yvon, F., Gallé, M., et al. Bloom: A 176b-parameter open-access multilingual language model. *arXiv preprint arXiv:2211.05100*, 2022.
- Shaw, P., Uszkoreit, J., and Vaswani, A. Self-attention with relative position representations. *arXiv preprint arXiv:1803.02155*, 2018.
- Su, J., Lu, Y., Pan, S., Murtadha, A., Wen, B., and Liu, Y. Roformer: Enhanced transformer with rotary position embedding. *arXiv preprint arXiv:2104.09864*, 2021.
- Thompson, L. and Mimno, D. Topic modeling with contextualized word representation clusters. *arXiv preprint arXiv:2010.12626*, 2020.
- Touvron, H., Martin, L., Stone, K., Albert, P., Almahairi, A., Babaei, Y., Bashlykov, N., Batra, S., Bhargava, P., Bhosale, S., et al. Llama 2: Open foundation and fine-tuned chat models. *arXiv preprint arXiv:2307.09288*, 2023.
- Trockman, A. and Kolter, J. Z. Mimetic initialization of self-attention layers. *arXiv preprint arXiv:2305.09828*, 2023.
- Tsai, Y.-H. H., Bai, S., Yamada, M., Morency, L.-P., and Salakhutdinov, R. Transformer dissection: a unified understanding of transformer’s attention via the lens of kernel. *arXiv preprint arXiv:1908.11775*, 2019.
- Vaswani, A., Shazeer, N., Parmar, N., Uszkoreit, J., Jones, L., Gomez, A. N., Kaiser, Ł., and Polosukhin, I. Attention is all you need. *Advances in neural information processing systems*, 30, 2017.
- Vershynin, R. *High-dimensional probability: An introduction with applications in data science*, volume 47. Cambridge university press, 2018.
- Vig, J. and Belinkov, Y. Analyzing the structure of attention in a transformer language model. *arXiv preprint arXiv:1906.04284*, 2019.
- Wang, B., Shang, L., Lioma, C., Jiang, X., Yang, H., Liu, Q., and Simonsen, J. G. On position embeddings in bert. In *International Conference on Learning Representations*, 2020.
- Wang, K., Variengien, A., Conmy, A., Shlegeris, B., and Steinhardt, J. Interpretability in the wild: a circuit for indirect object identification in gpt-2 small. *arXiv preprint arXiv:2211.00593*, 2022.
- Wang, Y.-A. and Chen, Y.-N. What do position embeddings learn? an empirical study of pre-trained language model positional encoding. *arXiv preprint arXiv:2010.04903*, 2020.
- Yamamoto, Y. and Matsuzaki, T. Absolute position embedding learns sinusoid-like waves for attention based on relative position. In *Proceedings of the 2023 Conference on Empirical Methods in Natural Language Processing*, pp. 15–28, 2023.
- Yeh, C., Chen, Y., Wu, A., Chen, C., Viégas, F., and Wattenberg, M. Attentionviz: A global view of transformer attention. *arXiv preprint arXiv:2305.03210*, 2023.
- Zhao, P. and Yu, B. On model selection consistency of lasso. *The Journal of Machine Learning Research*, 7:2541–2563, 2006.

# Appendix

## Table of Contents

<b>A Models, datasets, and implementations</b>	<b>17</b>
A.1 Pretrained models . . . . .	17
A.2 Training small transformers . . . . .	18
A.3 Removing artifacts . . . . .	18
A.4 Positional basis calculation . . . . .	18
<b>B Additional empirical results for Section 2</b>	<b>19</b>
B.1 Comparison with original sinusoidal positional embedding . . . . .	19
B.2 Do residual connections explain consistent geometry? . . . . .	19
<b>C Additional empirical results for Section 3</b>	<b>20</b>
C.1 PCA visualization . . . . .	20
C.2 Low rank measurements . . . . .	20
C.3 On cluster structure . . . . .	20
<b>D Additional empirical results for Section 4</b>	<b>25</b>
D.1 On robustness of positional basis . . . . .	25
D.2 On sparse and local attention . . . . .	25
D.3 On Addition experiments . . . . .	25
<b>E Additional empirical results for Section 5</b>	<b>32</b>
E.1 On trained weight matrix . . . . .	32
E.2 On enhanced QK/attention visualization . . . . .	32
<b>F Proofs for theoretical results</b>	<b>32</b>
F.1 Proof of Theorem 1 . . . . .	35
F.2 Proof of Theorem 2 . . . . .	38

## A Models, datasets, and implementations

We present the details of our experiments and measurements.

### A.1 Pretrained models

We downloaded and used pretrained models from Huggingface. In addition, we trained a [NanoGPT](#) on a [Shakespeare](#) dataset and on addition tasks.

- GPT-2 ([Radford et al., 2019](#)): 12-layer, 12-head, 768-dim, 124M parameters, autoregressive, absolute positional encoding at 0th-layer, pretrained on OpenWebText;

- BERT (Devlin et al., 2018): 12-layer, 12-head, 768-dim, 124M parameters, masked prediction, absolute positional encoding at 0th-layer, pretrained on BooksCorpus and English Wikipedia;
- BLOOM (Scao et al., 2022): 24-layer, 16-head, 1024-dim, 560M parameters, ALiBI positional encodings (Press et al., 2021) at each layer, pretrained on 45 natural languages and 12 programming languages;
- Llama2-7B (Touvron et al., 2023): 32-layer, 32-head, 4096-dim, 7B parameters, autoregressive, Rotary positional embedding (Su et al., 2021) at every layer, pretrained on a variety of data.

Note that (i) the training objective for pretraining BERT is different from the other models, and (ii) Llama 2 uses rotary positional encoding for each layer and BLOOM uses ALiBI positional encoding—which is different from absolute positional encoding that is added at the 0-th layer (Vaswani et al., 2017).

## A.2 Training small transformers

We train a few smaller transformers in this paper. Models are based on the GPT-2 architecture with adjusted parameters, and we adopt the implementation of the [GitHub Project](#) by Andrej Karpathy. The hardware we use is mainly RTX3090ti. All the following experiments take under 1 hour to train.

- **NanoGPT in Table 1 and 2:** The model is a vanilla Transformer with 6 layers, 6 heads, 384 dimensional embeddings, residual/embedding/attention dropout set to 0.1, weight decay set to 0.1, and a context window of 128. The dataset is Shakespeare with character-level tokenization. We train 5000 iterations using the AdamW optimizer, with a batch size of 64 and a cosine scheduler (100 step warmup) up to a learning rate of  $1e-3$ ;
- **Addition:** Similarly, we use a vanilla Transformer with 4 layers, 4 heads, 256 dimensional embeddings, and weight decay set to 0.1. The context window is set as the length of the longest sequence, i.e., 33 for the 10-digits addition task here. We train 10,000 iterations using the AdamW optimizer, with a batch size 64 and a linear scheduler up to a learning rate of  $1e-4$ .

## A.3 Removing artifacts

There are two likely artifacts in the measurements and visualization that we removed in the paper.

1. First token in a sequence. We find that a large proportion of attention is focused on the first token, which usually distorts visualization significantly. It has been known that the first token functions as a “null token”, which is removed in analysis (Vig & Belinkov, 2019). We also adopt removing the first token in our measurements and visualization.
2. Final-layer embeddings. We find that the embeddings of the final layer typically do not have a significant positional basis component. It is likely that positional information is no longer needed since last-layer embeddings are directly connected to the loss function.

## A.4 Positional basis calculation

We calculate positional bases based on sampled sequences of length  $T$  from a subset of the corpus, which includes OpenWebText, WikiText, and GitHub. The implementation and weights of the pretrained models are obtained from HuggingFace.

For the curated corpus subset, we utilize the streaming version of the HuggingFace datasets and extract the first 10K samples from the train split. Then we tokenize the dataset using the same tokenizer employed



by the pretrained model. The size of the final datasets vary across tasks and datasets, and we ensure that there are at least 1M tokens in each case to prevent the occurrence of overlapping sequences.

We set the context window  $T = 512$  for BERT, BLOOM, and GPT-2, as this maintains the maximum context window utilized during pretraining. For Llama-2, we set  $T = 512$  instead of a longer maximum sequence length due to computational resource limitations.

## B Additional empirical results for Section 2

### B.1 Comparison with original sinusoidal positional embedding

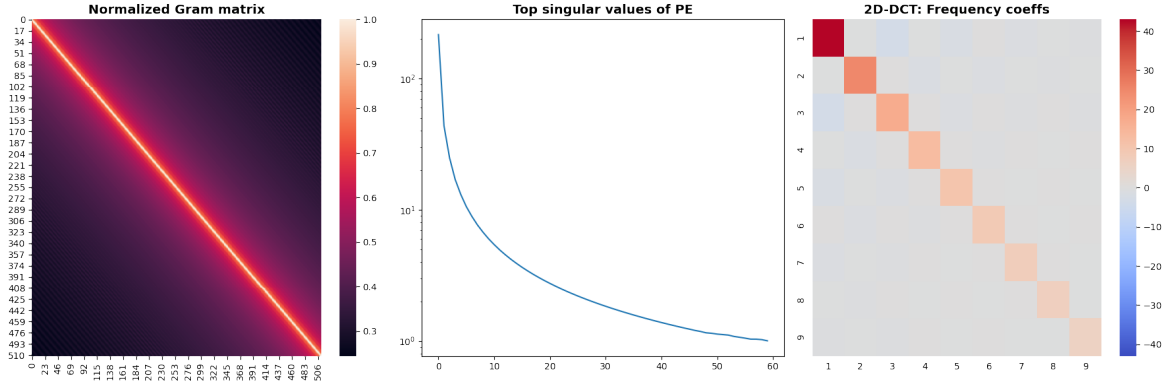


Figure 7: **Original sinusoidal positional embedding** proposed in Vaswani et al. (2017) is fixed. Compare the spectral and Fourier plots with Figure 3 and Figure 2.

The original sinusoidal positional embedding (PE) proposed in Vaswani et al. (2017) is fixed:

$$[\mathbf{pos}_t]_i = \begin{cases} \sin\left(\frac{t}{10000^{2i/d}}\right), & i = 2k \\ \cos\left(\frac{t}{10000^{2i/d}}\right), & i = 2k + 1 \end{cases}$$

Although this PE and learned positional basis both have sinusoidal patterns, we observe differences by comparing Figure 7 and Figure 3 and 2:

1. The Gram matrix of learned positional basis is visually smooth, whereas the original PE has large spiky values in the diagonal.
2. The learned positional basis has a more pronounced low-rank structure, as there is a sharper drop of top singular values.
3. The learned positional basis has more low-frequency 2D Fourier coefficients.

### B.2 Do residual connections explain consistent geometry?

The residual connections in transformers provide an identity mapping across layers, which may seem to be a plausible reason for the consistency of observed geometry in Section 2.

We show evidence that this is not the case. We use pretrained GPT-2 to generate embeddings by feeding the transformer with random tokens of length 512 uniformly sampled from the vocabulary. Then, we calculate the average norm of embeddings in each layer, and the cosine similarity of embeddings between every two layers.

In Figure 8, we find

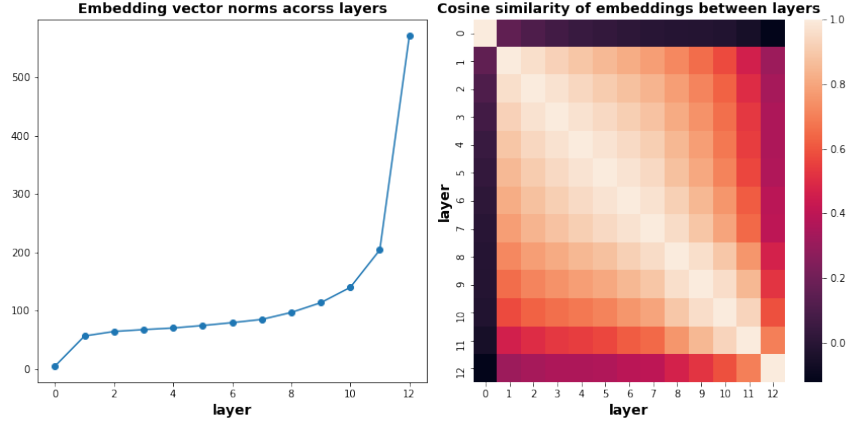


Figure 8: **Average embedding norm and cosine similarity** from GPT-2 based on a random sampled sequence.

1. The embedding norms increase significantly across layers. In particular, the norm ratio between Layer 1 and Layer 0 is 10.92, and between final layer and Layer 0 is 109.8.
2. The cosine similarity between the 0-th layer and any other layer is close to 0, which indicates that embeddings experience dramatic changes from Layer 0 to Layer 1.

These observations imply that residual connections cannot explain the consistent geometry in Section 2.

## C Additional empirical results for Section 3

We provide visualization and analysis for models other than GPT-2.

### C.1 PCA visualization

See Figure 9—Figure 14. Note: BERT displays a more complex circular shape, likely because its training objective is different from the others.

### C.2 Low rank measurements

We provide rank estimates for all layers.

**Rank estimate.** We report the rank estimate for all pretrained models and datasets in Table 4. Additionally, we include another rank estimate—the Stable rank estimate (Rudelson & Vershynin, 2007) in Table 5.

**Relative norm.** We report the relative norm for all pretrained models and datasets in Table 6.

### C.3 On cluster structure

See Figure 15—Figure 17. The bottom right part of the normalized Gram matrix, namely `ctx-ctx` part, exhibit progressively clear block structures. Four blocks indicate that there are 4 clusters among all `ctx` vectors—which correspond to exactly 4 documents we sample the sequences from.

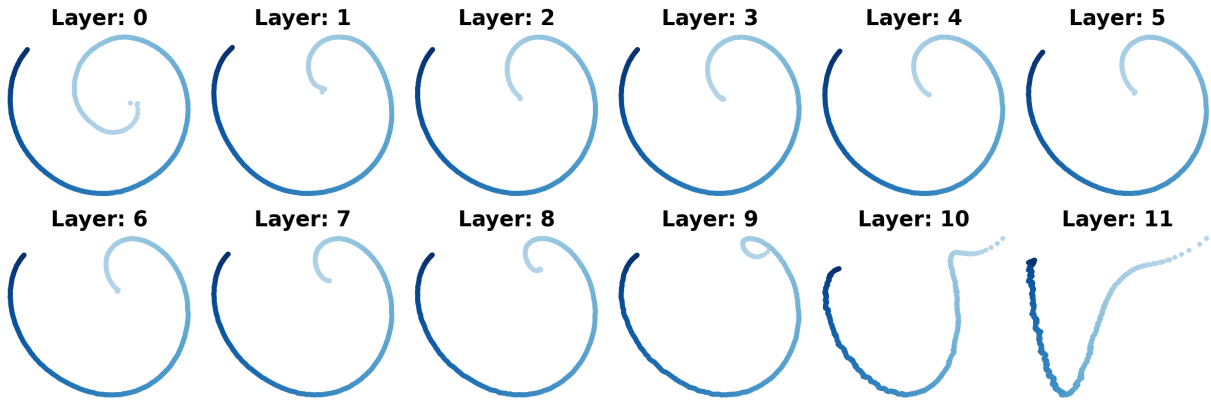


Figure 9: Top-2 principal components of positional basis; GitHub, GPT2

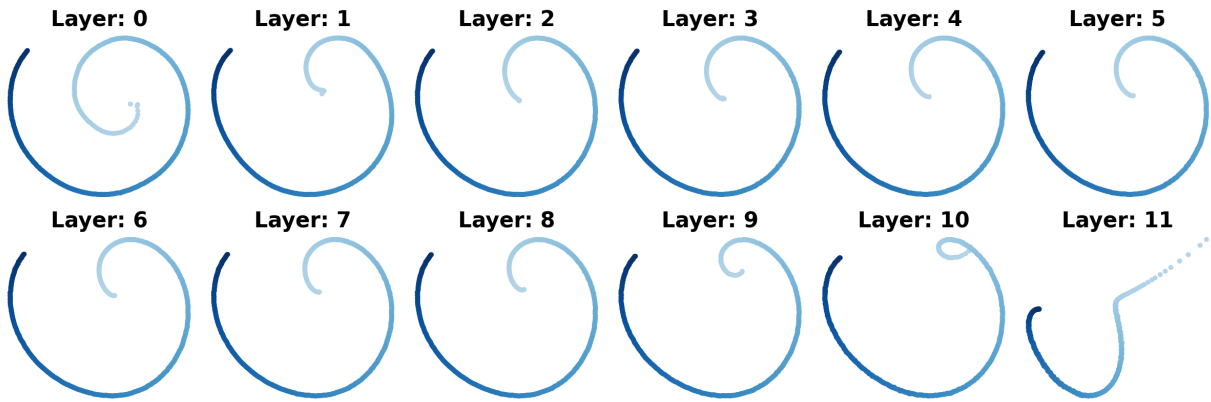


Figure 10: Top-2 principal components of positional basis; WikiText, GPT2

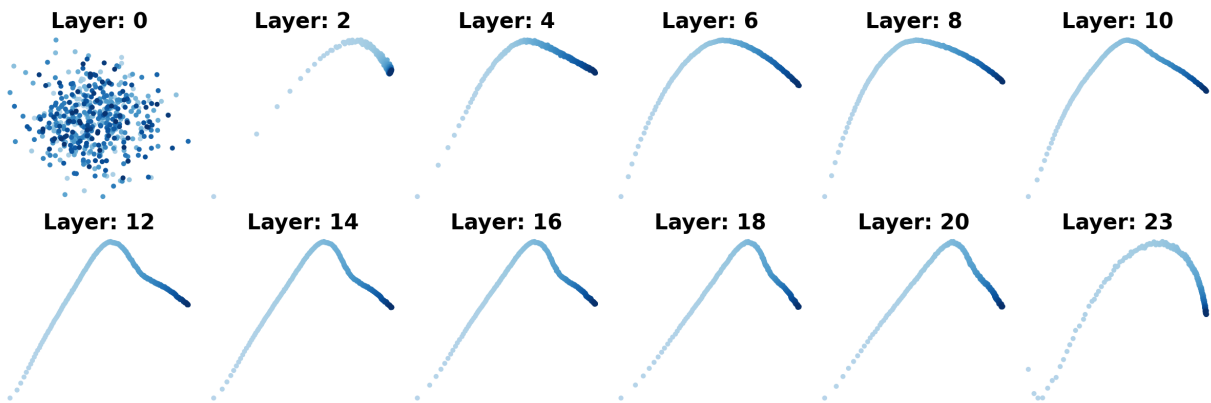


Figure 11: Top-2 principal components of positional basis; OpenWebText, BLOOM

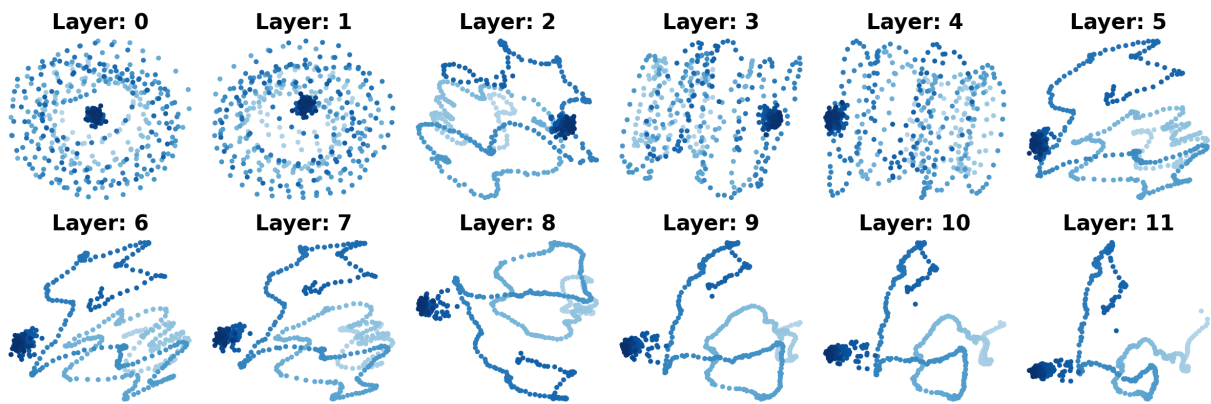


Figure 12: Top-2 principal components of positional basis; OpenWebText, BERT

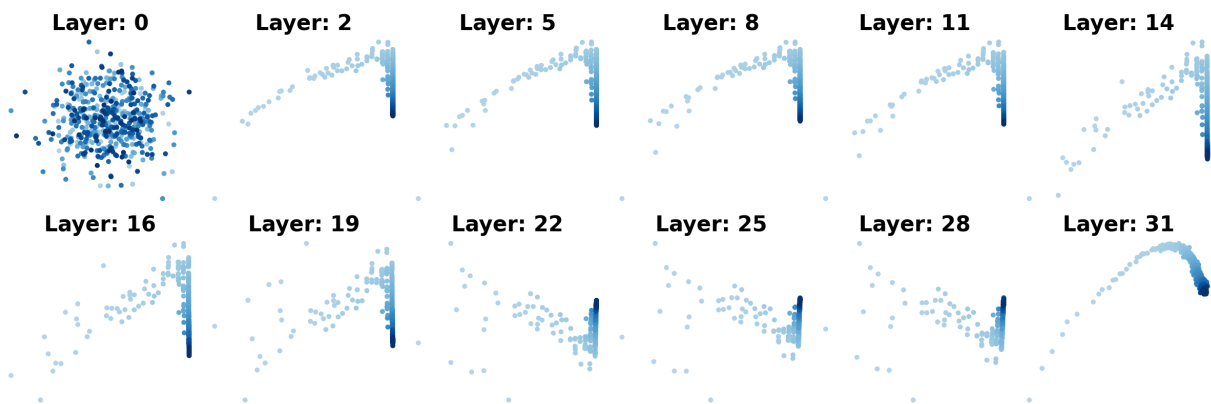


Figure 13: Top-2 principal components of positional basis; OpenWebText, Llama2

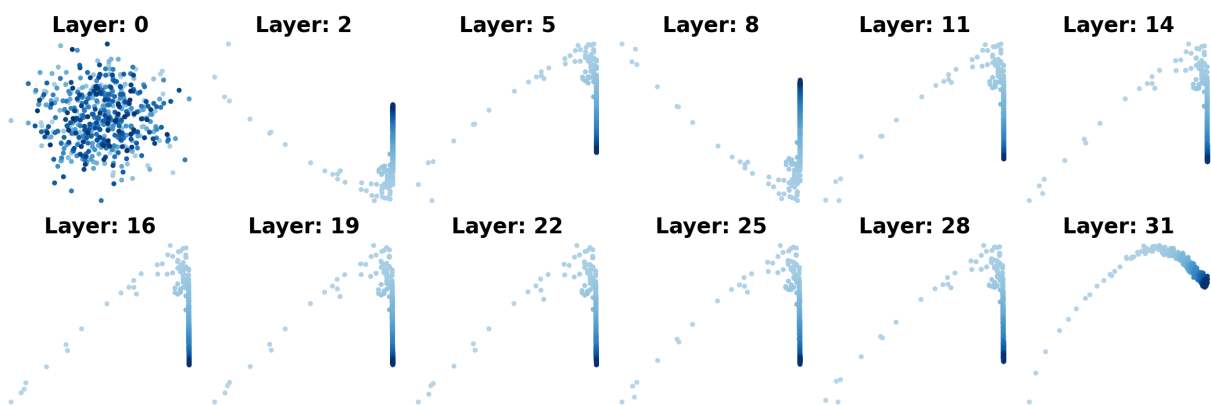


Figure 14: Top-2 principal components of positional basis; GitHub, Llama2

Table 4: ScreeNOT Rank Estimate for models, datasets and at each layer.

		Layer 0	Layer 1	Layer 2	Layer 3	Layer 4	Layer 5	Layer 6	Layer 7	Layer 8	Layer 9	Layer 10	Layer 11	Layer 12
BERT	GitHub	15	16	16	16	14	11	11	9	10	10	11	11	12
	OpenWebText	15	16	18	16	11	11	9	9	11	11	11	11	13
	WikiText	15	16	18	16	12	11	9	9	11	11	11	12	12
BLOOM	GitHub	8	9	9	8	9	10	10	11	10	10	10	10	10
	OpenWebText	6	10	10	11	11	10	11	11	11	11	10	10	11
	WikiText	6	8	9	10	10	11	11	11	11	11	11	10	11
GPT2	GitHub	15	14	13	12	12	11	11	10	10	10	11	11	10
	OpenWebText	15	13	14	12	13	11	10	10	10	10	9	9	12
	WikiText	15	14	14	12	11	11	11	11	11	11	9	10	12
Llama2	GitHub	6	10	9	8	10	8	8	9	9	9	9	8	10
	OpenWebText	7	10	10	11	11	10	9	10	9	8	9	8	10
	WikiText	8	10	10	10	9	8	8	8	8	8	8	8	10

Table 5: Stable rank for models, datasets and at each layer.

		Layer 0	Layer 1	Layer 2	Layer 3	Layer 4	Layer 5	Layer 6	Layer 7	Layer 8	Layer 9	Layer 10	Layer 11	Layer 12
BERT	GitHub	9.19	7.79	5.26	4.73	4.34	3.84	3.48	3.20	2.70	2.45	2.04	1.84	1.91
	OpenWebText	9.19	7.63	5.25	4.73	4.10	3.53	3.16	2.84	2.46	2.30	2.18	2.22	2.15
	WikiText	9.19	7.78	5.03	4.58	3.99	3.48	3.14	2.82	2.42	2.27	2.13	2.16	2.12
BLOOM	GitHub	8.39	1.25	1.20	1.21	1.21	1.23	1.29	1.29	1.28	1.25	1.21	1.02	1.00
	OpenWebText	8.33	1.27	1.30	1.24	1.24	1.27	1.32	1.34	1.33	1.26	1.16	1.01	1.00
	WikiText	8.42	1.27	1.28	1.30	1.31	1.34	1.41	1.43	1.41	1.32	1.22	1.01	1.00
GPT2	GitHub	2.05	1.92	1.91	1.89	1.90	1.90	1.92	1.94	1.98	2.03	2.05	1.70	1.11
	OpenWebText	2.05	1.92	1.91	1.89	1.88	1.88	1.88	1.90	1.91	1.96	2.02	2.24	1.49
	WikiText	2.05	1.92	1.91	1.89	1.88	1.88	1.88	1.90	1.91	1.97	2.03	2.19	1.56
Llama2	GitHub	24.87	1.00	1.00	1.00	1.00	1.00	1.01	1.01	1.01	1.01	1.02	1.03	1.17
	OpenWebText	52.23	1.00	1.00	1.00	1.00	1.00	1.01	1.01	1.02	1.02	1.03	1.05	1.44
	WikiText	24.70	1.00	1.00	1.01	1.01	1.02	1.03	1.05	1.09	1.16	1.20	1.26	1.30

Table 6: Relative norm for models, datasets and at each layer.

		Layer 0	Layer 1	Layer 2	Layer 3	Layer 4	Layer 5	Layer 6	Layer 7	Layer 8	Layer 9	Layer 10	Layer 11	Layer 12
BERT	GitHub	0.445	0.483	0.569	0.616	0.648	0.707	0.764	0.786	0.768	0.686	0.631	0.562	0.473
	OpenWebText	0.465	0.546	0.660	0.759	0.877	0.977	0.973	0.967	0.953	0.901	0.777	0.658	0.596
	WikiText	0.454	0.502	0.626	0.695	0.798	0.916	0.968	0.965	0.949	0.887	0.756	0.682	0.627
BLOOM	GitHub	0.013	0.123	0.232	0.279	0.343	0.385	0.343	0.306	0.301	0.306	0.325	0.219	0.181
	OpenWebText	0.012	0.138	0.194	0.264	0.315	0.342	0.297	0.267	0.264	0.300	0.392	0.575	0.589
	WikiText	0.013	0.149	0.222	0.287	0.328	0.352	0.336	0.301	0.295	0.325	0.407	0.494	0.491
GPT2	GitHub	0.999	0.994	0.996	0.972	0.812	0.762	0.672	0.600	0.489	0.442	0.386	0.303	0.123
	OpenWebText	1.000	0.996	0.990	0.989	0.986	0.983	0.981	0.979	0.974	0.841	0.631	0.480	0.075
	WikiText	1.000	0.995	0.991	0.989	0.987	0.986	0.984	0.981	0.981	0.933	0.680	0.555	0.110
Llama2	GitHub	0.029	0.221	0.221	0.222	0.222	0.222	0.223	0.223	0.224	0.225	0.226	0.227	0.183
	OpenWebText	0.038	0.146	0.146	0.146	0.147	0.147	0.148	0.148	0.150	0.152	0.154	0.154	0.148
	WikiText	0.034	0.060	0.060	0.060	0.060	0.061	0.062	0.063	0.065	0.068	0.072	0.076	0.191

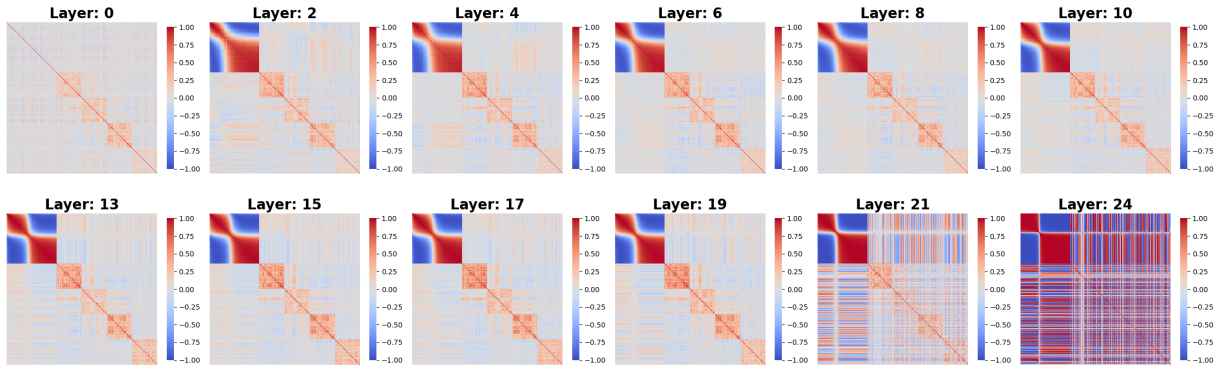


Figure 15: Gram matrix of positional basis and context basis; Openwebtext, BLOOM

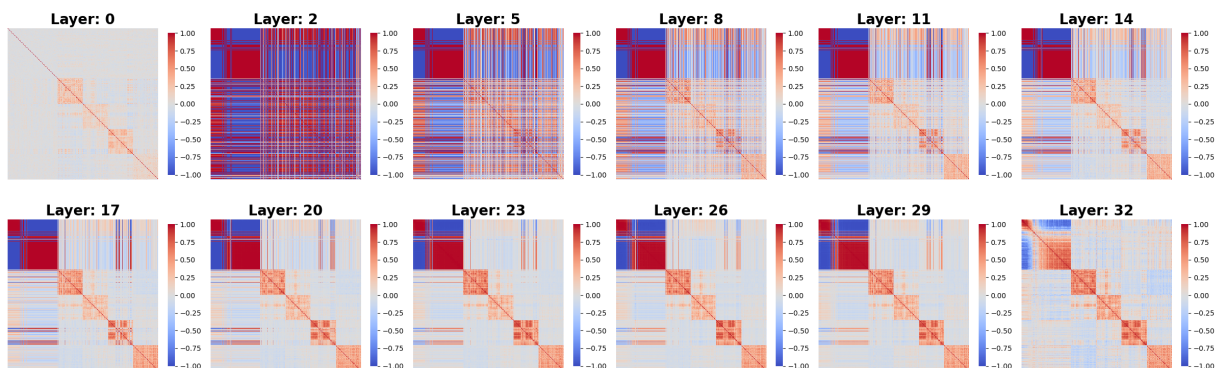


Figure 16: Gram matrix of positional basis and context basis; Openwebtext, Llama2

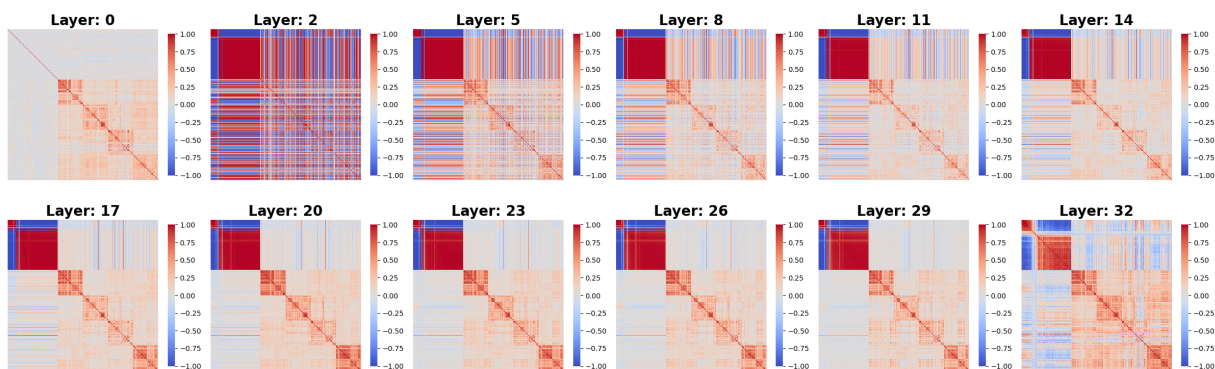


Figure 17: Gram matrix of positional basis and context basis; GitHub, Llama



## D Additional empirical results for Section 4

### D.1 On robustness of positional basis

In Table 2, we sampled OOD sequences to test if positional basis is robust and reported the ratio explained by top-10 frequencies.

Here we provide a visual examination, which further confirms that positional basis possesses similar low-rank and spiral structure. We choose BLOOM, which has been pretrained on both natural languages and programming languages, and we use random sampled tokens to test whether its associated positional basis still has similar structure.

We find that similar structure persists even for the above randomly sampled sequences. See Figure 24.

### D.2 On sparse and local attention

Here we provide evidence that the argmax property (8) is satisfied in GPT-2 at a substantial level. We consider a variant of pos-pos QK constituent matrix  $\tilde{P}W\tilde{P}^\top$  where each column of  $\tilde{P}$  is  $\text{pos}_t + \mu$ , because we find the global mean  $\mu$  helps satisfy this argmax property.

Note that checking this pos-pos QK constituent instead of the QK matrix is more straightforward: pos-pos QK constituent reflects the property of the model and positional basis, without needing the context information.

For each layer and each head, we calculate  $\tilde{P}W\tilde{P}^\top$  and examine the fraction of positions  $t$  such that

$$\arg \max_{t' \leq t} [\tilde{P}W\tilde{P}^\top]_{t,t'} = t.$$

Figure 25 shows the ratios for each layer and head. It is clear that this argmax property is mostly satisfied in many heads, especially among early layers.

### D.3 On Addition experiments

We have manually generated the addition dataset. The number of digits of the addition ranges from 5 to 10, and is sampled under uniform distribution in the training process. The model achieve above 99% accuracy on training set and in-distribution test set. However, the model does not achieve length generalization. It achieves 32.6%, 8.0%, 11.1%, and 9.9% accuracy on 1k samples of addition with digits length 1, 2, 3, 4 respectively.

**Similar findings for transformers with relative embedding.** Additionally, we implement a rotary-embedding based model by replacing the absolute positional embedding with RoPE Su et al. (2021). For the rotary-embedding based model, the corresponding accuracy is 35.6%, 13.4%, 20.0%, 38.5%.

**Visualizing discontinuity.** We plot the QK matrices and Gram matrices for both transformers—with absolute embedding and with rotary position embedding. See Figure 18—Figure 23. Notice that the unsmoothness is pervasive in the Gram matrix of positional basis and QK matrix **across different layers, heads, and models**.

**Quantitative measurements.** We calculated the ratios that low-frequency components can explain in the Fourier space at various layers and heads. The lack of smoothness is further confirmed by the Fourier analysis.



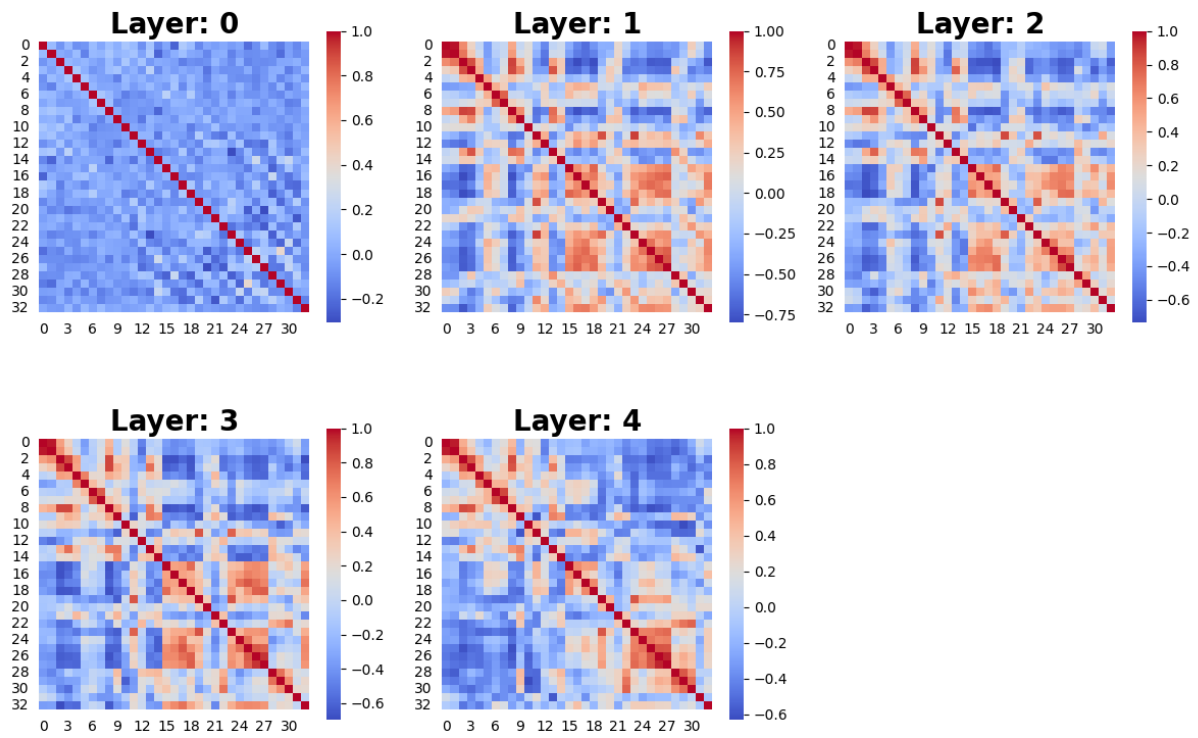


Figure 18: Gram matrix of positional basis; **Addition** with absolute PE shows nonsmoothness.

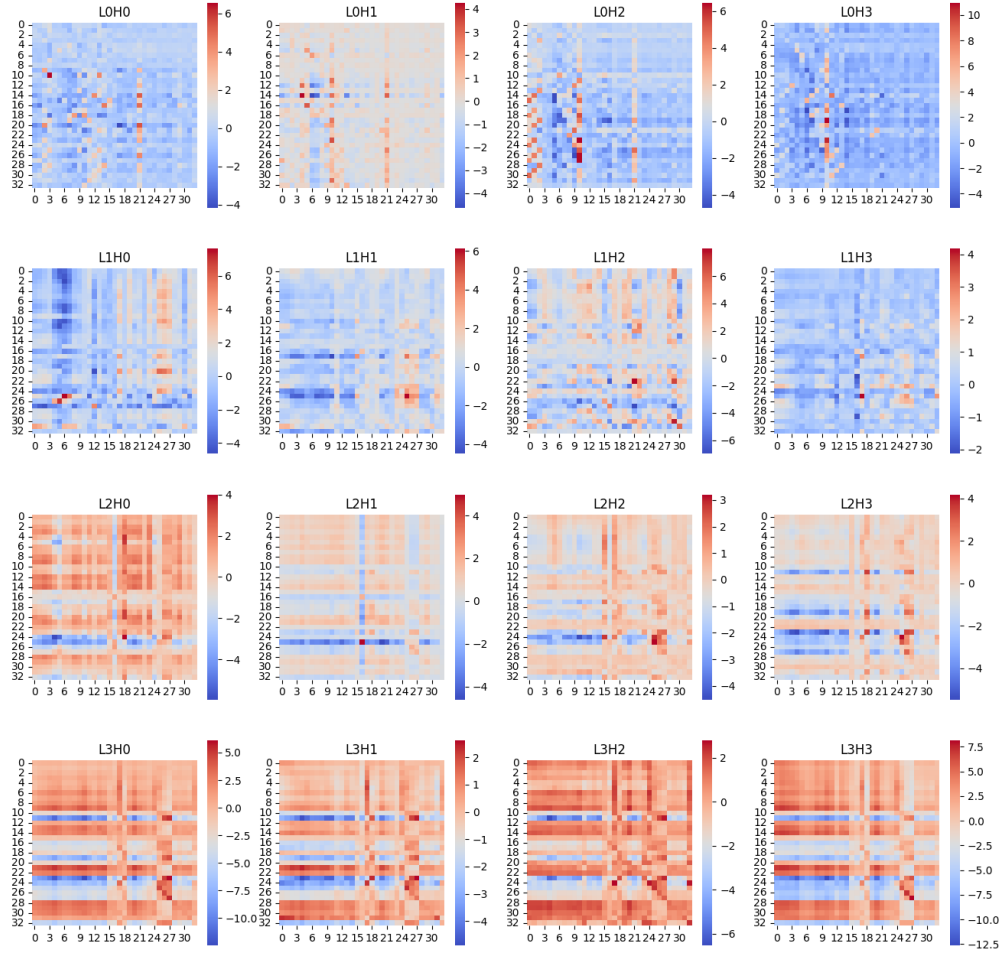


Figure 19: QK matrix of positional basis; **Addition** with absolute PE shows nonsmoothness.

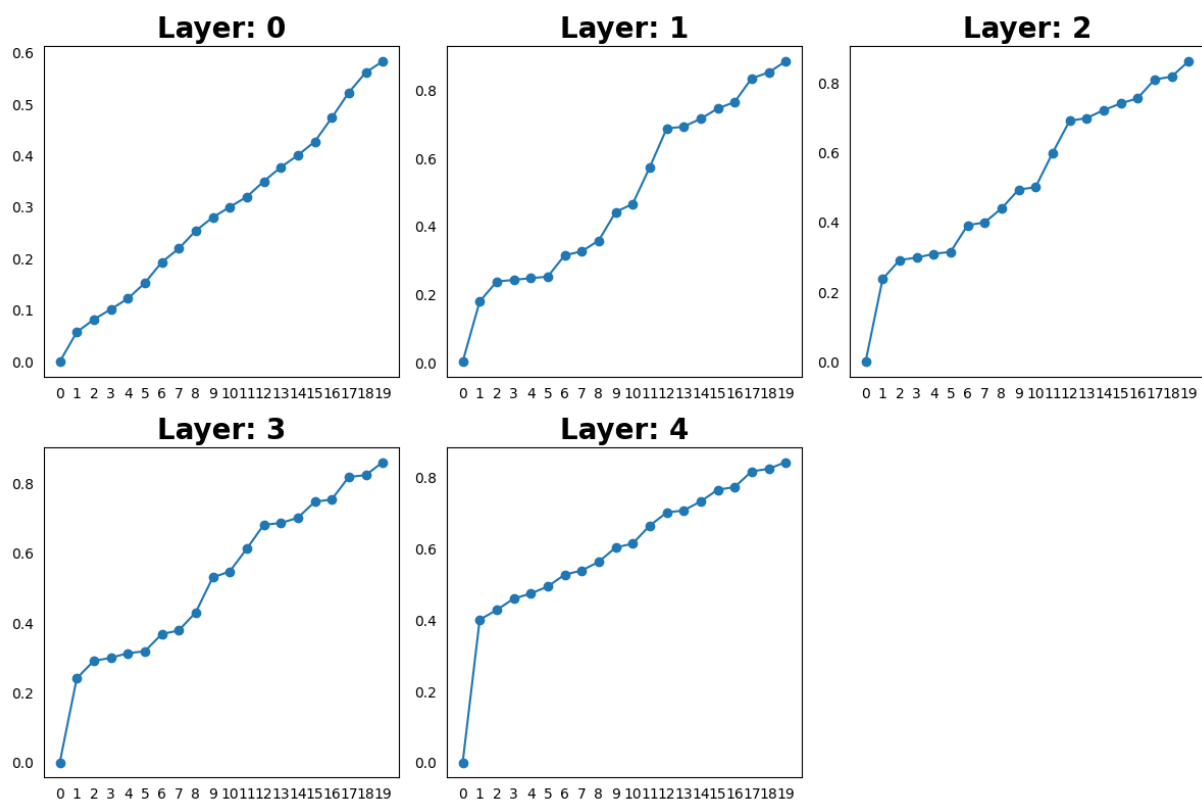


Figure 20: Fourier of positional basis; **Addition** with absolute PE depends on higher-frequency components.

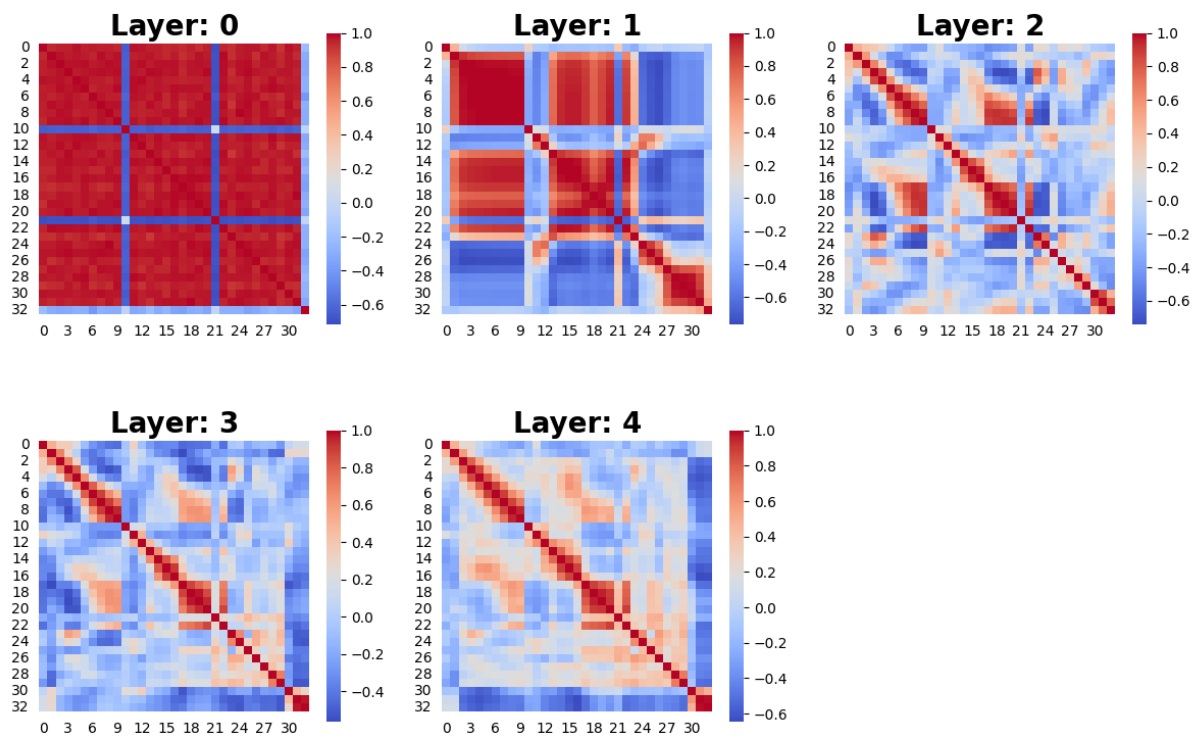


Figure 21: Fourier of positional basis; **Addition** with rotary PE shows nonsmoothness.

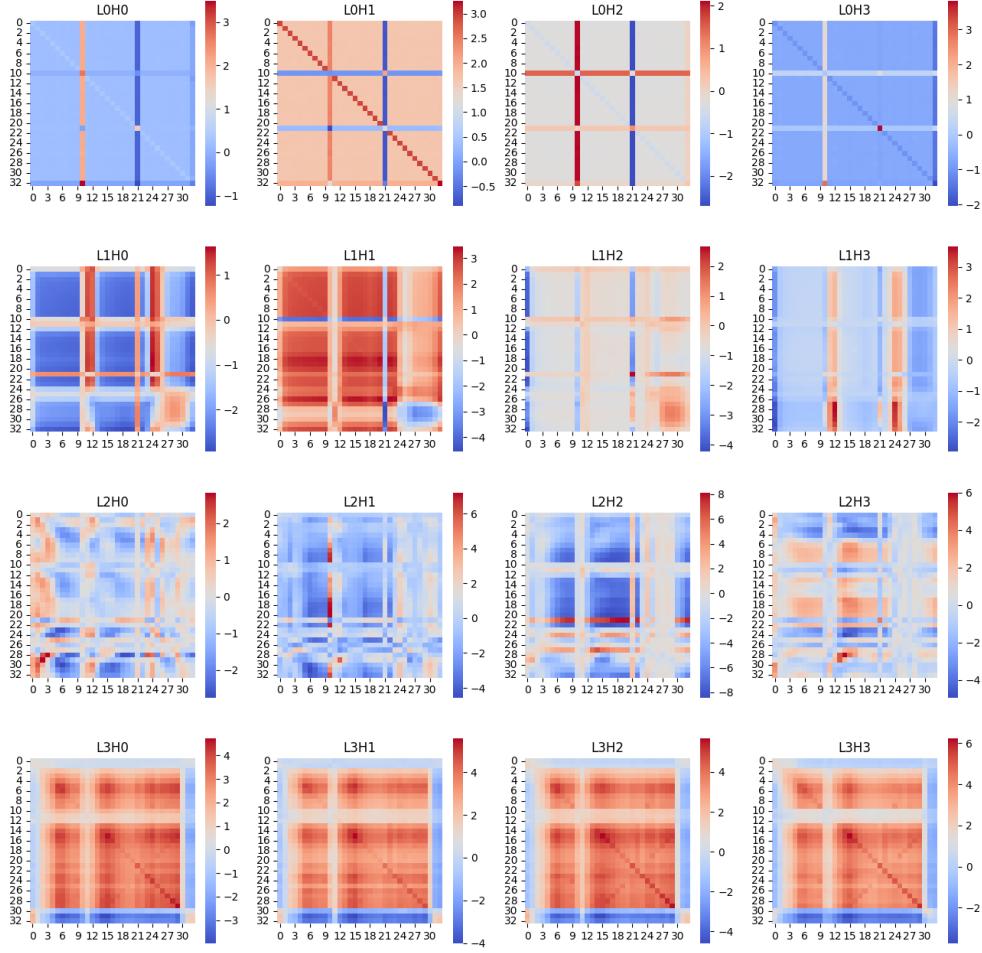


Figure 22: QK matrix of positional basis; **Addition** with absolute PE shows nonsmoothness.

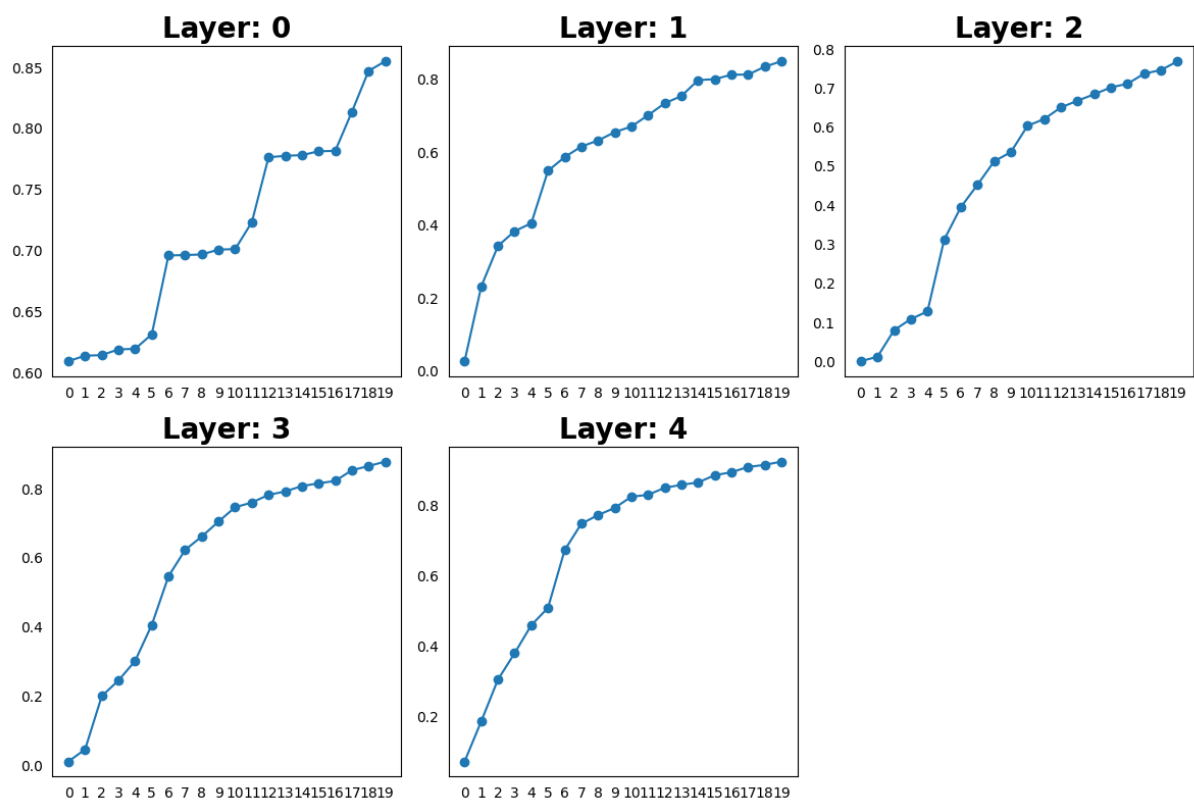


Figure 23: Fourier of positional basis; **Addition** with absolute PE depends on higher-frequency components.

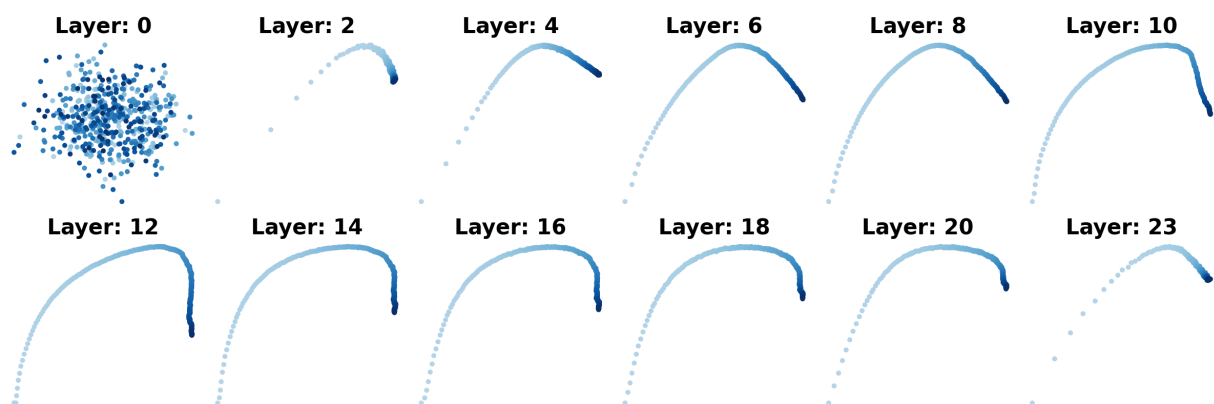


Figure 24: Top-2 PC plot of positional basis ; Bloom on random tokens

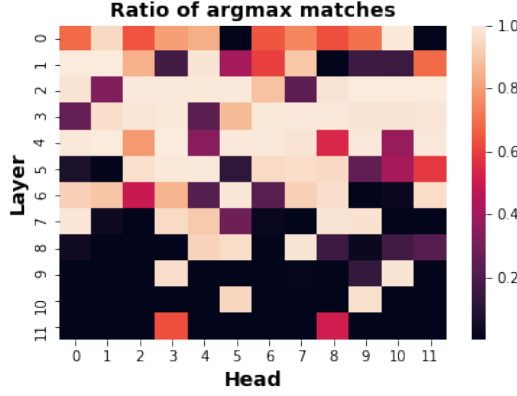


Figure 25: **Ratio of positions that satisfy the argmax property (8).**

## E Additional empirical results for Section 5

### E.1 On trained weight matrix

We provide decomposition of trained weight matrices similar to Figure 4. See Figure 26—Figure 29 for more plots about  $W = W^q(W^k)^\top / \sqrt{d_{\text{head}}}$  at various layers and heads for BERT and GPT-2 model.

### E.2 On enhanced QK/attention visualization

**On global mean vector.** We show the QK matrix decomposition with global mean (Figure 30), and without global mean (Figure 31). Note that adding a constant to all entries of the QK matrix will not change the attention matrix, because softmax computes the ratio. We conclude that the global mean vector  $\mu$  has little effect on interpretations.

**Visualizing QK constituents.** We use the QK decomposition (10) to provide fine-grained visualization for attention heads. In Figure 32—Figure 34, we select various heads on GPT-2 and BLOOM model and provide 6 subplots based on (i) the 4 QK constituents, (ii) the original QK matrix, and (iii) the attention matrix.

We find that visualization based on individual QK constituents provides additional information beyond visualizing the attention matrix alone. Our selection of heads is representative, as many similar heads appear in GPT-2 and BLOOM.

## F Proofs for theoretical results

We introduce some additional notations. Denote the indicator function by  $\mathbf{1}$ . We denote by  $\mathbf{1}_N$  the vector  $(1, 1, \dots, 1)^\top \in \mathbb{R}^N$ . For a complex matrix  $A$ , we denote the conjugate transpose by  $A^*$ . For convenience, for a matrix  $A$ , we will write  $\Delta A$  instead of  $\Delta^{(1,1)} A$ . For a vector  $x \in \mathbb{C}^N$ , we also write  $\Delta x$  to denote the finite difference vector  $N \cdot (x_1 - x_0, x_2 - x_1, \dots, x_N - x_{N-1})^\top$  (where  $x_N = x_0$ ). We will say that a Hermitian matrix  $A \in \mathbb{C}^{N \times N}$  is positive semidefinite (PSD) if and only if  $x^* A x \geq 0$  for every  $x \in \mathbb{C}^N$ . Denote by  $\Re(x)$  the real part of a complex number  $x \in \mathbb{C}$ .



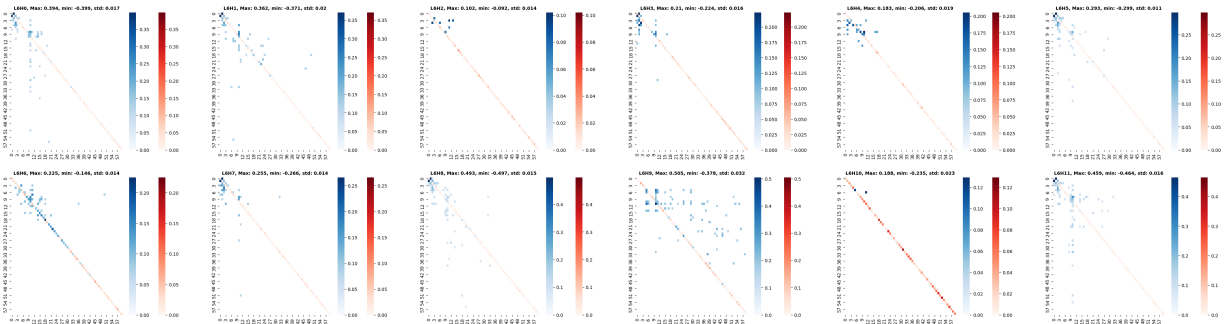


Figure 26: Dissecting attention weights, GPT2 L6

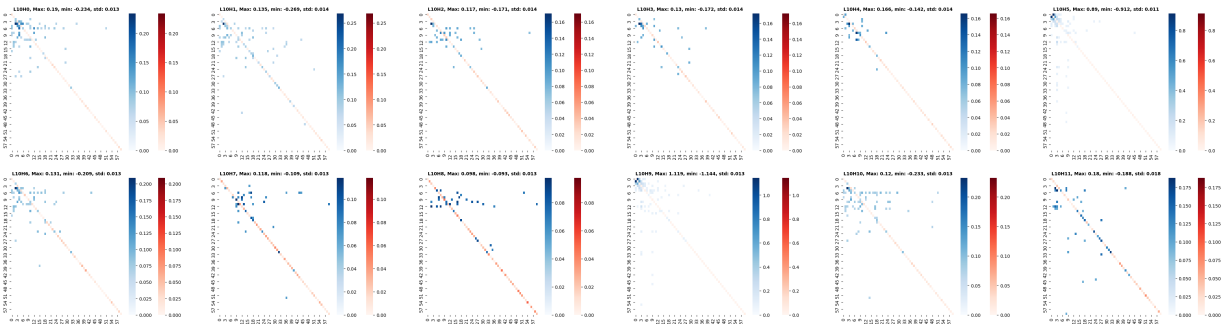


Figure 27: Dissecting attention weights, GPT2 L10

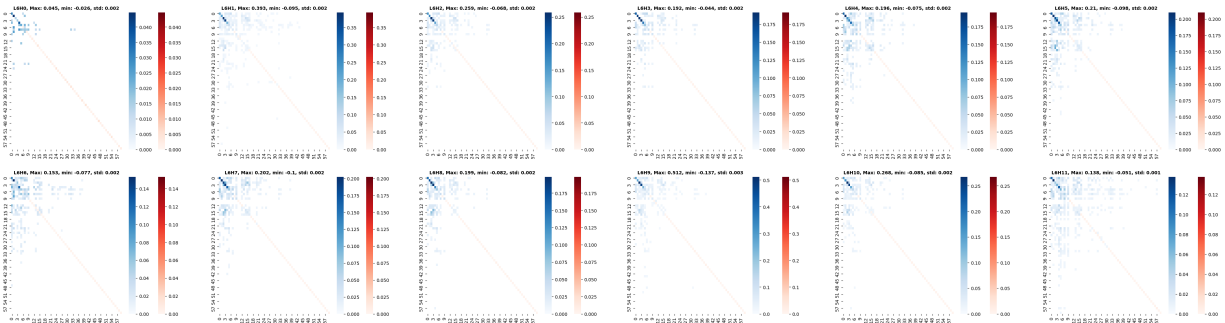


Figure 28: Dissecting attention weights, BERT L6

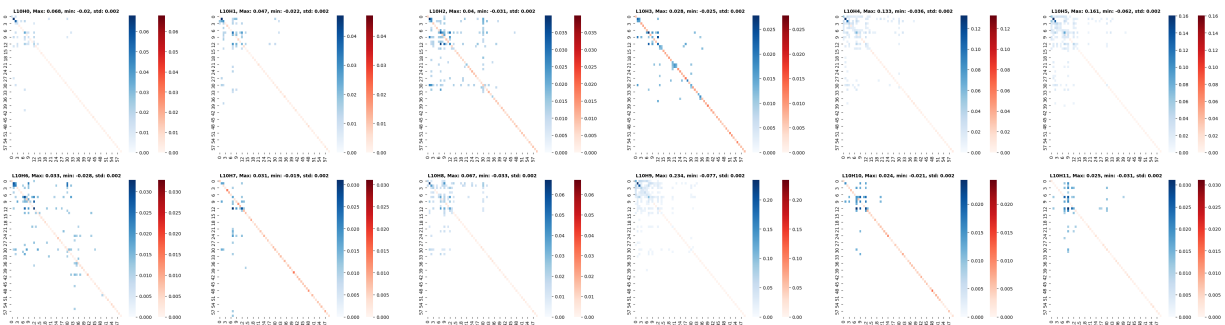


Figure 29: Dissecting attention weights, BERT L10

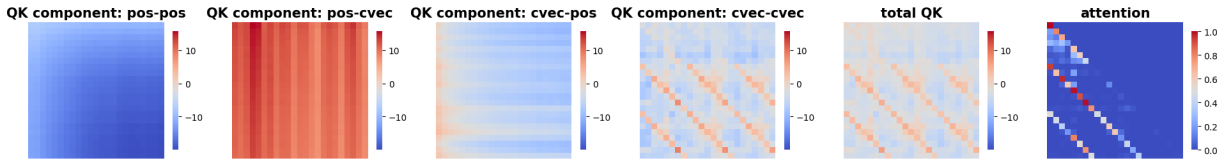


Figure 30: QK matrix decomposition with global mean; GPT2, Layer 10 Head 7

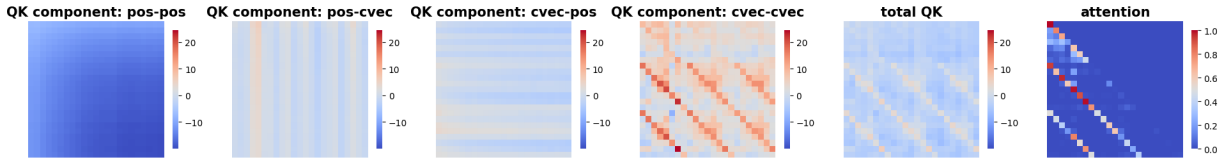


Figure 31: QK matrix decomposition without global mean; GPT2, Layer 10 Head 7

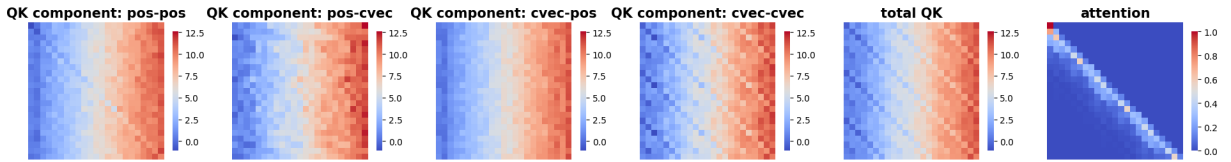


Figure 32: QK Decomposition; BLOOM L10H1

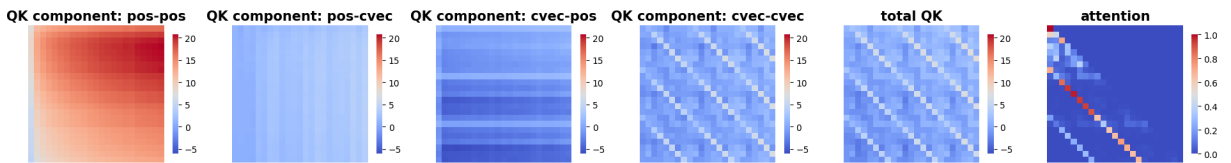


Figure 33: QK Decomposition; BLOOM L7H6

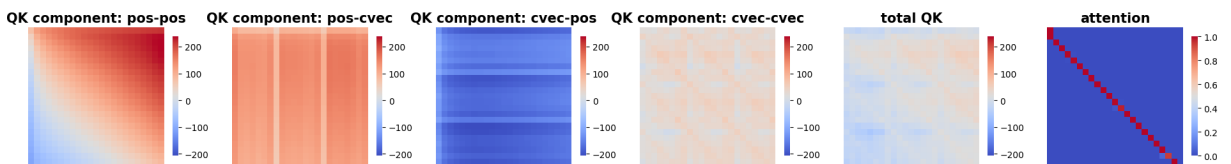


Figure 34: QK Decomposition; GPT2 L4H11

## F.1 Proof of Theorem 1

In this subsection, we denote a generic dimension by  $N$  and  $\omega = \exp(-2\pi i/N)$ . We need some standard definitions and properties; see [Broughton & Bryan \(2018\)](#) for example.

The discrete Fourier transform (DFT) matrix  $\mathbf{F} \in \mathbb{C}^{N \times N}$  is given by  $F_{tt'} = \omega^{(t-1)(t'-1)}$  for  $1 \leq t, t' \leq N$ . The inverse discrete Fourier transform (IDFT) matrix is  $N^{-1}\mathbf{F}^*$ . Both the DFT matrix and the IDFT matrix are symmetric (not Hermitian). Sometimes we prefer to write  $\mathbf{F}^\top$  instead of  $\mathbf{F}$  simply for formality. For a generic matrix  $\mathbf{A} \in \mathbb{R}^{N \times N}$ , we denote by  $\hat{\mathbf{A}} \in \mathbb{C}^{N \times N}$  the matrix after its 2-d DFT. It satisfies

$$\begin{aligned}\hat{\mathbf{A}} &= \mathbf{F}\mathbf{A}\mathbf{F}^\top, \\ \mathbf{A} &= N^{-2}\mathbf{F}^*\hat{\mathbf{A}}(\mathbf{F}^*)^\top.\end{aligned}\tag{15}$$

The following simple lemma is a consequence of integration-by-parts for the discrete version. For completeness we include a proof.

**Lemma 1.** *Let  $\mathbf{x} \in \mathbb{R}^N$  be a vector, and  $\hat{\mathbf{x}} = \mathbf{F}\mathbf{x}$  be its DFT. Then for  $t = 1, \dots, N$ ,*

$$\hat{x}_t = \gamma_t(\mathbf{F}\Delta\mathbf{x})_t + \mathbf{1}\{t=1\} \cdot \sum_{t'=1}^N x_{t'}, \quad \text{where} \tag{16}$$

$$\gamma_t := N^{-1} \left( 1 - \exp\left(\frac{-2\pi i(t-1)}{N}\right) \right)^{-1} \quad \text{for } t > 1 \text{ and } \gamma_1 := 1. \tag{17}$$

*Proof.* If  $t = 1$ , then  $(\mathbf{F}\mathbf{x})_t = \sum_{t'=1}^N x_{t'}$ , and  $(\mathbf{F}\Delta\mathbf{x})_t = N \sum_{t'=1}^N (x_{t'} - x_{t'-1}) = 0$ . For  $t \neq 1$ ,

$$\begin{aligned}(\mathbf{F}\Delta\mathbf{x})_t &= N \sum_{t'=1}^N \omega^{(t-1)(t'-1)} (x_{t'} - x_{t'-1}) = N \sum_{t'=1}^N (\omega^{(t-1)(t'-1)} - \omega^{(t-1)t'}) x_{t'} \\ &= N(1 - \omega^{(t-1)}) \sum_{t'=1}^N \omega^{(t-1)(t'-1)} x_{t'} = \gamma_t^{-1}(\mathbf{F}\mathbf{x})_t.\end{aligned}$$

This shows  $\hat{x}_t = \gamma_t(\mathbf{F}\Delta\mathbf{x})_t$  for  $t \neq 1$  and completes the proof.  $\square$

A simple bound on the modulus  $|\gamma_t|$  is given by the following lemma.

**Lemma 2.** *Let  $\gamma_t$  be defined by (17). For positive integer  $1 < t \leq N/2$ , we have*

$$|\gamma_{N-t+2}| = |\gamma_t| \leq \frac{1}{8(t-1)}.$$

*Proof.* The equality part is obvious. For any  $\theta \in (-\pi, \pi)$ , we have

$$|1 - \exp(i\theta)|^2 = (1 - \cos\theta)^2 + \sin^2\theta = 4\sin^2(\theta/2) = 4\sin^2(|\theta|/2)$$

Since  $\sin\theta/\theta$  is monotone decreasing in  $(0, \pi/2)$ , we have  $\sin(|\theta|/2) \geq \sin(\pi/2)|\theta|/(\pi/2)$ . Thus,

$$|1 - \exp(i\theta)| \geq 4|\theta|/\pi.$$

Setting  $\theta = -2\pi(t-1)/N$ , we obtain the desired upper bound on  $|\gamma_t|$ .  $\square$

Denote  $\mathbf{\Gamma} = \text{diag}\{\gamma_1, \dots, \gamma_N\}$ . By Lemma 1, for any vector  $\mathbf{x} \in \mathbb{R}^N$ ,

$$\mathbf{F}\mathbf{x} = \mathbf{\Gamma}\mathbf{F}\Delta\mathbf{x} + \begin{pmatrix} \mathbf{x}^\top \mathbf{1}_N \\ 0 \\ \vdots \\ 0 \end{pmatrix}.$$

Below we will assume that the generic matrix  $\mathbf{A} \in \mathbb{R}^{N \times N}$  is symmetric and satisfies  $\mathbf{A}\mathbf{1}_N = \mathbf{0}$ . Observe that

$$\begin{aligned} \mathbf{F}\mathbf{A} &= [\mathbf{F}\mathbf{A}_{:,1}, \dots, \mathbf{F}\mathbf{A}_{:,N}] = \mathbf{\Gamma}\mathbf{F}[\Delta\mathbf{A}_{:,1}, \dots, \Delta\mathbf{A}_{:,N}], \\ \mathbf{F}\mathbf{A}\mathbf{F}^\top &= \mathbf{\Gamma}\mathbf{F}(\Delta\mathbf{A})\mathbf{F}^\top \mathbf{\Gamma} \end{aligned}$$

where we used  $\mathbf{A}\mathbf{1}_N = \mathbf{0}$  and  $(\Delta\mathbf{A})\mathbf{1}_N = \mathbf{0}$ . Repeating the second equality  $m$  times, we obtain

$$\hat{\mathbf{A}} = \mathbf{F}\mathbf{A}\mathbf{F}^\top = \mathbf{\Gamma}^m \mathbf{F}(\Delta^{(m,m)}\mathbf{A})\mathbf{F}^\top \mathbf{\Gamma}^m.$$

Now fix a generic nonempty index sets  $\mathcal{I} \subset \{1, 2, \dots, N\}$  and denote  $\mathcal{J} = \{1, \dots, N\} \setminus \mathcal{I}$ . Consider the block matrix form of  $\hat{\mathbf{A}}$ :

$$\hat{\mathbf{A}} = \begin{pmatrix} \hat{\mathbf{A}}_{\mathcal{I},\mathcal{I}} & \hat{\mathbf{A}}_{\mathcal{I},\mathcal{J}} \\ \hat{\mathbf{A}}_{\mathcal{J},\mathcal{I}} & \hat{\mathbf{A}}_{\mathcal{J},\mathcal{J}} \end{pmatrix}.$$

Using the block matrix notation, we derive

$$\|\hat{\mathbf{A}}_{\mathcal{I},\mathcal{J}}\|_{\text{op}} = \|\mathbf{\Gamma}_{\mathcal{I},\mathcal{I}}^m (\mathbf{F}(\Delta^{(m,m)}\mathbf{A})\mathbf{F}^\top)_{\mathcal{I},\mathcal{J}} \mathbf{\Gamma}_{\mathcal{J},\mathcal{J}}^m\|_{\text{op}} \leq \max_{t \in \mathcal{I}, t' \in \mathcal{J}} |\gamma_t \gamma_{t'}|^m \|\mathbf{F}(\Delta^{(m,m)}\mathbf{A})\mathbf{F}^\top\|_{\text{op}}.$$

Similar inequalities hold for other three blocks. By Lemma 2 we have  $|\gamma_t| \leq 1$  for all  $t$ . Adding the three inequalities that involve at least one index set  $\mathcal{J}$ , we get

$$\left\| \hat{\mathbf{A}} - \begin{pmatrix} \hat{\mathbf{A}}_{\mathcal{I},\mathcal{I}} & \mathbf{0} \\ \mathbf{0} & \mathbf{0} \end{pmatrix} \right\|_{\text{op}} \leq 3 \max_{t \in \mathcal{J}} |\gamma_t|^m \|\mathbf{F}(\Delta^{(m,m)}\mathbf{A})\mathbf{F}^\top\|_{\text{op}}.$$

Since  $\mathbf{F}\mathbf{F}^* = N$ , we have  $\|\mathbf{F}\|_{\text{op}} = \|\mathbf{F}\mathbf{F}^*\|_{\text{op}}^{1/2} = N^{1/2}$ . Denoting

$$\mathbf{A}^{(\text{res})} := N^{-2} \mathbf{F}^* \left[ \hat{\mathbf{A}} - \begin{pmatrix} \hat{\mathbf{A}}_{\mathcal{I},\mathcal{I}} & \mathbf{0} \\ \mathbf{0} & \mathbf{0} \end{pmatrix} \right] (\mathbf{F}^*)^\top,$$

we find

$$\|\mathbf{A}^{(\text{res})}\|_{\text{op}} \leq 3 \max_{t \in \mathcal{J}} |\gamma_t|^m N^{-2} \|\mathbf{F}\|_{\text{op}}^4 \|\Delta^{(m,m)}\mathbf{A}\|_{\text{op}} \leq 3 \max_{t \in \mathcal{J}} |\gamma_t|^m N \|\Delta^{(m,m)}\mathbf{A}\|_{\text{max}} \quad (18)$$

where the first inequality is due to Lemma 2 and the second inequality is due to the inequality between matrix operator norm and max norm.

To finish the proof, let us make some specification: we identify  $N$  with  $\tilde{T}$  (namely  $2T$ ), identify  $\mathbf{A}$  with  $\tilde{\mathbf{G}}$ , and identify  $\mathcal{I} = \{1, \dots, k\} \cup \{\tilde{T} - k + 1, \dots, \tilde{T}\}$ . These choices satisfy the requirement for  $\mathbf{A}$  because  $\tilde{\mathbf{G}}$  is symmetric and it satisfies  $\tilde{\mathbf{G}}\mathbf{1}_{\tilde{T}} = 2\mathbf{G}\mathbf{1}_T = \mathbf{0}$  due to the assumption  $\text{pos}_1 + \dots + \text{pos}_T = \mathbf{0}$ .

By Lemma 2,  $\max_{t \in \mathcal{J}} |\gamma_t| \leq 1/(8k)$ , so (18) gives

$$\|\mathbf{A}^{(\text{res})}\|_{\text{op}} \leq 6(8k)^{-m} T \|\Delta^{(m,m)}\tilde{\mathbf{G}}\|_{\text{max}}$$

By the definition of  $\mathbf{A}^{(\text{res})}$  and the identities in 15,

$$\tilde{\mathbf{G}} = \mathbf{A}^{(\text{res})} + N^{-2} \mathbf{F}^* \begin{pmatrix} \hat{\mathbf{A}}_{\mathcal{I},\mathcal{I}} & \mathbf{0} \\ \mathbf{0} & \mathbf{0} \end{pmatrix} (\mathbf{F}^*)^\top.$$

We make the following claim.

**Lemma 3.** *There exists  $\mathbf{B} \in \mathbb{R}^{k \times k}$  such that*

$$N^{-2} \left[ \mathbf{F}^* \begin{pmatrix} \hat{\mathbf{A}}_{\mathcal{I}, \mathcal{I}} & \mathbf{0} \\ \mathbf{0} & \mathbf{0} \end{pmatrix} (\mathbf{F}^*)^\top \right]_{1:T, 1:T} = \mathbf{F}_{\leq k} \mathbf{B} (\mathbf{F}_{\leq k} \mathbf{B})^\top \quad (19)$$

While the DFT matrix is complex, the above lemma claims that the left-hand side is a Gram matrix of real low-frequency vectors. Once this lemma is proved, we can combine this lemma with (18) and  $\mathbf{G} = \tilde{\mathbf{G}}_{1:T, 1:T}$  to obtain the desired inequality 1 in Theorem 1.

*Proof of Lemma 3.* Recall  $\omega = \exp(-2\pi i/2T)$ . We further introduce some notations. Denote  $\mathcal{I}_1 = \{1, \dots, k\}$  and  $\mathcal{I}_2 = \{T - k + 1, \dots, T\}$  so that  $\mathcal{I} = \mathcal{I}_1 \cup \mathcal{I}_2$ . Let  $q_t = \omega^{t-1}$  for positive integer  $t$ , matrix  $\mathbf{Q} \in \mathbb{R}^{T \times k}$  and matrix  $\mathbf{D} \in \mathbb{R}^{k \times k}$  be given by

$$Q_{t,s} = \Re(q_t^{s-0.5}), \quad \text{where } t \leq T, s \leq k, \quad \mathbf{D} = \text{diag}(q_1^{1/2}, \dots, q_k^{1/2})$$

For  $t, t' \in \mathcal{I}$ ,

$$\begin{aligned} \hat{A}_{t,t'} &= (\mathbf{F} \mathbf{A} \mathbf{F}^T)_{t,t'} \\ &= \sum_{s,s'=1}^T F_{t,s} G_{s,s'} F_{t',s'} + \sum_{s,s'=1}^T F_{t,2T+1-s} G_{s,s'} F_{t',s'} \\ &\quad + \sum_{s,s'=1}^T F_{t,s} G_{s,s'} F_{t',2T+1-s'} + \sum_{s,s'=1}^T F_{t,2T+1-s} G_{s,s'} F_{t',2T+1-s'} \\ &= q_t^{1/2} q_{t'}^{1/2} \sum_{s,s'=1}^T G_{s,s'} \left( q_t^{s-0.5} q_{t'}^{s'-0.5} + q_t^{-s+0.5} q_{t'}^{s'-0.5} + q_t^{s-0.5} q_{t'}^{-s'+0.5} + q_t^{-s+0.5} q_{t'}^{-s'+0.5} \right) \\ &= 4q_t^{1/2} q_{t'}^{1/2} \sum_{s,s'=1}^T G_{s,s'} \Re(q_t^{s-1/2}) \Re(q_{t'}^{s'-1/2}). \end{aligned}$$

If  $t, t' \in \mathcal{I}_1$ , the above equation leads to

$$\hat{A}_{\mathcal{I}_1, \mathcal{I}_1} = 4\mathbf{D} \mathbf{Q}^\top \mathbf{G} \mathbf{Q} \mathbf{D};$$

and more generally  $\hat{A}_{\mathcal{I}, \mathcal{I}}$  is given by symmetrically extending  $\hat{A}_{\mathcal{I}_1, \mathcal{I}_1}$  as in the definition of  $\tilde{\mathbf{G}}$ . Since  $4\mathbf{Q}^\top \mathbf{G} \mathbf{Q}$  is a PSD, we can find  $\mathbf{B}_0 \in \mathbb{R}^{k \times k}$  such that

$$4\mathbf{Q}^\top \mathbf{G} \mathbf{Q} = \mathbf{B}_0 \mathbf{B}_0^\top.$$

We want to simplify  $\mathbf{F}_{:, \mathcal{I}}^* \hat{\mathbf{A}}_{\mathcal{I}, \mathcal{I}} \mathbf{F}_{\mathcal{I}, :}^*$ , namely

$$\mathbf{F}_{:, \mathcal{I}_1}^* \hat{\mathbf{A}}_{\mathcal{I}_1, \mathcal{I}_1} \mathbf{F}_{\mathcal{I}_1, :}^* + \mathbf{F}_{:, \mathcal{I}_1}^* \hat{\mathbf{A}}_{\mathcal{I}_1, \mathcal{I}_2} \mathbf{F}_{\mathcal{I}_2, :}^* + \mathbf{F}_{:, \mathcal{I}_2}^* \hat{\mathbf{A}}_{\mathcal{I}_2, \mathcal{I}_1} \mathbf{F}_{\mathcal{I}_1, :}^* + \mathbf{F}_{:, \mathcal{I}_2}^* \hat{\mathbf{A}}_{\mathcal{I}_2, \mathcal{I}_2} \mathbf{F}_{\mathcal{I}_2, :}^* \quad (20)$$

For any  $t, t' \in \mathcal{I}_1$ ,

$$(\mathbf{F}^*)_{t, \mathcal{I}_1} \hat{\mathbf{A}}_{\mathcal{I}_1, \mathcal{I}_1} (\mathbf{F}^*)_{\mathcal{I}_1, t'} = (\mathbf{F}^*)_{t, \mathcal{I}_1} \mathbf{D} \mathbf{B}_0 \mathbf{B}_0^\top \mathbf{D} (\mathbf{F}^*)_{\mathcal{I}_1, t'}$$

and similar equations hold for other three cases. Observe that

$$(\mathbf{F}^*)_{t, \mathcal{I}_1} \mathbf{D} = (\bar{q}_t^{1-0.5}, \dots, \bar{q}_t^{k-0.5}), \quad (\mathbf{F}^*)_{t, \mathcal{I}_2} \mathbf{D} = (\bar{q}_t^{2T-0.5}, \dots, \bar{q}_t^{2T-k+0.5}).$$

When we add the four terms in 20, the imaginary part cancels out. Thus,

$$\mathbf{F}_{t, \mathcal{I}}^* \hat{\mathbf{A}}_{\mathcal{I}, \mathcal{I}} \mathbf{F}_{\mathcal{I}, t'}^* = 4 \left( \Re(\bar{q}_t^{1-0.5}), \dots, \Re(\bar{q}_t^{k-0.5}) \right) \mathbf{B}_0 \mathbf{B}_0^\top \left( \Re(\bar{q}_t^{1-0.5}), \dots, \Re(\bar{q}_t^{k-0.5}) \right)^\top.$$

Note that  $\Re(\bar{q}_t^{s-0.5}) = \cos(\pi(t-1)(s-0.5)/T) = (\mathbf{F}_{\leq k})_{t,s}$ . Expressing  $\mathbf{F}_{:, \mathcal{I}}^* \hat{\mathbf{A}}_{\mathcal{I}, \mathcal{I}} \mathbf{F}_{\mathcal{I}, :}^*$  in the matrix form and denote  $\mathbf{B} = \mathbf{B}_0/N$ , we find that (19) holds.  $\square$

## F.2 Proof of Theorem 2

First we note that

$$K_{\mathbf{W}}(\mathbf{x}^q, \mathbf{x}^k) = K_{\mathbf{W}_{11}}(\mathbf{x}^q, \mathbf{x}^k) K_{\mathbf{W}_{12}}(\mathbf{x}^q, \mathbf{x}^k) K_{\mathbf{W}_{21}}(\mathbf{x}^q, \mathbf{x}^k) K_{\mathbf{W}_{22}}(\mathbf{x}^q, \mathbf{x}^k). \quad (21)$$

We will prove that

$$K_{\mathbf{W}_{11}}(\mathbf{x}^q, \mathbf{x}^k) = (1 + O(\text{incoh})) \cdot K_{\mathbf{W}_{11}}(\mathbf{c}^q, \mathbf{c}^k). \quad (22)$$

To prove this, it suffices to show that

$$\max \{K_{\mathbf{W}_{11}}(\mathbf{c}^q, \mathbf{t}^k), K_{\mathbf{W}_{11}}(\mathbf{t}^q, \mathbf{c}^k), K_{\mathbf{W}_{11}}(\mathbf{t}^q, \mathbf{t}^k)\} = 1 + O(\text{incoh}). \quad (23)$$

We decompose  $\mathbf{W}_{11}$  as in (13) and find

$$\log \left( K_{\mathbf{W}_{11}}(\mathbf{c}^q, \mathbf{t}^k) \right) = (\mathbf{c}^q)^\top \mathbf{W}_{11} \mathbf{t}^k = \sum_{k=1}^s a_k (\mathbf{u}_k^\top \mathbf{c}^q) (\mathbf{v}_k^\top \mathbf{t}^k).$$

By mutual incoherence,  $|\mathbf{v}_k^\top \mathbf{t}^k| \leq \text{incoh}$  since  $\mathbf{v}_k \in \mathcal{B}_1$  and  $\mathbf{t}^k \in \mathcal{B}_2$ ; and trivially  $|\mathbf{u}_k^\top \mathbf{c}^k| \leq 1$ , so

$$\left| \log \left( K_{\mathbf{W}_{11}}(\mathbf{c}^q, \mathbf{t}^k) \right) \right| \leq \sum_{k=1}^s |\mathbf{u}_k^\top \mathbf{c}^k| \cdot |\mathbf{v}_k^\top \mathbf{t}^q| \leq s \cdot \text{incoh}.$$

Since by assumption  $s = O(1)$  and  $\exp(\text{incoh}) = 1 + O(\text{incoh})$ , we derive

$$K_{\mathbf{W}_{11}}(\mathbf{c}^q, \mathbf{t}^k) = 1 + O(\text{incoh}).$$

The other two terms in (23) follow a similar argument and thus are all bounded by  $1 + O(\text{incoh})$ . We can prove similarly that

$$\begin{aligned} K_{\mathbf{W}_{12}}(\mathbf{x}^q, \mathbf{x}^k) &= (1 + O(\text{incoh})) \cdot K_{\mathbf{W}_{12}}(\mathbf{c}^q, \mathbf{t}^k), \\ K_{\mathbf{W}_{21}}(\mathbf{x}^q, \mathbf{x}^k) &= (1 + O(\text{incoh})) \cdot K_{\mathbf{W}_{21}}(\mathbf{t}^q, \mathbf{c}^k), \\ K_{\mathbf{W}_{22}}(\mathbf{x}^q, \mathbf{x}^k) &= (1 + O(\text{incoh})) \cdot K_{\mathbf{W}_{22}}(\mathbf{t}^q, \mathbf{t}^k). \end{aligned}$$

and together with (22) and (21), this leads to the desired (14).

Below we prove the “moreover” part. By standard properties of independent subgaussian random variables (Vershynin, 2018, Sect. 2),  $(\mathbf{c}^q)^\top \mathbf{Z}_{11} \mathbf{t}^k$  is still a subgaussian random variable, and with probability at least  $1 - O(\exp(-\text{incoh}^2 \cdot d))$ , for certain constant  $C > 0$ ,

$$\left| \log \left( K_{\mathbf{W}_{11} + \mathbf{Z}/\sqrt{d}}(\mathbf{c}^q, \mathbf{t}^k) \right) \right| \leq s \cdot \text{incoh} + C \text{incoh} = O(\text{incoh}).$$

Similar high-probability bounds hold for other terms. By the union bound over all possible choice of vectors in  $\mathcal{B}_1^0$  and  $\mathcal{B}_2^0$ , we arrive at our claim.